Author Contributions:
Conceptualization: Luca Stirnimann, Thomas G. Bornman, Rosemary A. Dorrington, Sarah E. Fawcett
Data curation: Luca Stirnimann
Formal analysis: Luca Stirnimann
Funding acquisition: Thomas G. Bornman, Rosemary A. Dorrington, Sarah E. Fawcett

A Circum-Antarctic Plankton Isoscape: Carbon Export Potential Across the Summertime Southern Ocean

Luca Stirnimann[1] , Thomas G. Bornman[2,3] , Heather J. Forrer[1,4] , Joshua Mirkin[1] , Thomas J. Ryan-Keogh[5] , Raquel F. Flynn[1] , Rosemary A. Dorrington[6] , Hans M. Verheye[7] , and Sarah E. Fawcett[1,8]

[1]Department of Oceanography, University of Cape Town, Rondebosch, South Africa, [2]South African Environmental Observation Network, Gqeberha, South Africa, [3]Institute for Coastal and Marine Research, Nelson Mandela University, Gqeberha, South Africa, [4]Earth, Ocean and Atmospheric Science Department, Florida State University, Tallahassee, FL, USA, [5]Southern Ocean Carbon-Climate Observatory, Council for Scientific and Industrial Research, Cape Town, South Africa, [6]Department of Biochemistry and Microbiology, Rhodes University, Makhanda, South Africa, [7]Department of Biological Sciences, University of Cape Town, Rondebosch, South Africa, [8]Marine and Antarctic Research Centre for Innovation and Sustainability (MARIS), University of Cape Town, Rondebosch, South Africa

Abstract The Southern Ocean accounts for ~30% of the ocean's CO_2 sink, partly due to its biological pump that transfers surface-produced organic carbon to deeper waters. To estimate large-scale Southern Ocean carbon export potential and characterize its drivers, we measured the carbon and nitrogen isotope ratios of surface suspended particulate matter ($\delta^{13}C_{SPM}$, $\delta^{15}N_{SPM}$) for samples collected in summer 2016/2017 during the Antarctic Circumnavigation Expedition (364 stations). Concurrent measurements of phytoplankton community composition revealed the dominance of large diatoms in the Antarctic and nano-phytoplankton (mainly haptophytes) in open Subantarctic waters. As expected, $\delta^{13}C_{SPM}$ was strongly dependent on pCO_2, with local deviations in this relationship explained by phytoplankton community dynamics. $\delta^{15}N_{SPM}$ reflected the nitrogen sources consumed by phytoplankton, with higher inferred nitrate (versus recycled ammonium) dependence generally coinciding with higher micro-phytoplankton abundances. Using $\delta^{15}N_{SPM}$ and a two-endmember isotope mixing model, we quantified the extent of nitrate- versus ammonium-supported growth, which yields a measure of carbon export potential. We estimate that across the Southern Ocean, $41 \pm 29\%$ of the surface-produced organic carbon was potentially exported below the seasonal mixed layer during the growth season, with maximum export potential (50%–99%) occurring in the Antarctic Circumpolar Current's southern Boundary Zone and near the (Sub)Antarctic islands, reaching a minimum in the Subtropical Zone (<33%). Alongside iron, phytoplankton community composition emerged as an important driver of the Southern Ocean's biological pump, with large diatoms dominating regions characterized by high nitrate dependence and elevated carbon export potential and smaller, mainly non-diatom taxa proliferating in waters where recycled ammonium supported most productivity.

Plain Language Summary The Southern Ocean plays a crucial role in regulating climate by transferring atmospheric CO_2 to the deep ocean. This transfer is partly facilitated by the biological pump, which involves organic matter production by phytoplankton in surface waters and the subsequent sinking of some of this material into the deep ocean. To estimate the fraction of newly produced organic carbon potentially exported to depth (i.e., biological pump strength) and determine the drivers thereof, we measured the carbon and nitrogen isotope ratios of surface organic matter and characterized the phytoplankton community at high resolution around Antarctica in summer. We found that nearly half of the carbon produced by Southern Ocean phytoplankton during their growth season was potentially exported. The biological pump was strongest in the southernmost waters of the Antarctic Ocean and near the (Sub)Antarctic islands where local processes supplied iron to phytoplankton and large diatoms dominated the community. Export potential was weakest in open Southern Ocean waters where iron limitation was pervasive and smaller phytoplankton were dominant. While it is well known that iron exerts a strong control on the Southern Ocean's biological pump, our study highlights the complementary role of phytoplankton community composition in modulating carbon export.

AGU logo
AGU
ADVANCING EARTH
AND SPACE SCIENCES

Investigation: Thomas G. Bornman, Heather J. Forrer, Raquel F. Flynn
Methodology: Luca Stirnimann, Joshua Mirkin, Sarah E. Fawcett
Project Administration: Luca Stirnimann, Sarah E. Fawcett
Resources: Thomas G. Bornman, Thomas J. Ryan-Keogh, Sarah E. Fawcett
Supervision: Thomas G. Bornman, Hans M. Verheye, Sarah E. Fawcett
Writing – original draft: Luca Stirnimann, Sarah E. Fawcett
Writing – review & editing: Luca Stirnimann, Thomas G. Bornman, Heather J. Forrer, Thomas J. Ryan-Keogh, Raquel F. Flynn, Hans M. Verheye, Sarah E. Fawcett

1. Introduction

Phytoplankton are the foundation of marine food webs (Reynolds, 2006) and contribute to climate regulation by fixing CO_2 into organic carbon biomass (i.e., primary production; Falkowski et al., 1998). In the Southern Ocean, iron and light limitation of phytoplankton lead to mixed-layer macronutrient (i.e., nitrate and phosphate) concentrations that are perennially high (Martin et al., 1990; Sunda & Huntsman, 1997). Nonetheless, the Southern Ocean is a major contributor to the global ocean CO_2 sink, accounting for ∼30% of oceanic carbon uptake (Arteaga et al., 2018; DeVries, 2014; Frölicher et al., 2015). A key mechanism that maintains the surface-to-deep CO_2 gradient is the biological pump, which transfers a portion of the photosynthetically produced organic carbon into the ocean interior where it may be stored for hundreds of years (Volk & Hoffert, 1985).

Annually, ∼20% of net primary production (NPP) occurring in the Southern Ocean is exported from surface waters (Arteaga et al., 2018; Schlitzer, 2002). NPP and carbon export are elevated over the Antarctic continental shelf, near the (Sub)Antarctic islands, and in the marginal ice zone (MIZ), with the Ross and Weddell Seas emerging as productivity hotspots (Arrigo et al., 2008a, 2008b; Pollard et al., 2009; Schlitzer, 2002). Here, carbon production and export are thought to be enhanced because of local increases in the iron (and at times, silicic acid) supply and/or stratification (and thus higher light exposure) driven by seasonal ice melt (e.g., Death et al., 2014; Lannuzel et al., 2016). While experimental analyses, geochemical measurements, satellite data, and biogeochemical models have been used to investigate carbon export in the Southern Ocean (e.g., Fan et al., 2020; Hirawake et al., 2011; Kerkar et al., 2020), there remains a need for additional estimates based on in situ observations. Furthermore, to better predict how the Southern Ocean's biological pump and CO_2 sink may change requires an improved understanding of the drivers of carbon export at large scales (Henley et al., 2020).

The stable isotope ratios of carbon ($\delta^{13}C$, in ‰ vs. Vienna Pee Dee Belemnite (VPDB) = $[(({}^{13}C/{}^{12}C)_{sample}/({}^{13}C/{}^{12}C)_{VPDB})-1] \times 1,000$) and nitrogen ($\delta^{15}N$, in ‰ vs. N_2 in air = $[(({}^{15}N/{}^{14}N)_{sample}/({}^{15}N/{}^{14}N)_{air})-1] \times 1,000$) in suspended particulate matter (SPM) have been widely used to explore ecological and biogeochemical processes in the ocean. The $\delta^{13}C$ of phytoplankton biomass (often approximated by the $\delta^{13}C$ of SPM; $\delta^{13}C_{SPM}$) is set mainly by discrimination between the ${}^{12}C$ and ${}^{13}C$ isotopes (i.e., fractionation) during CO_2 diffusion across the cell membrane and its subsequent carboxylation (Fry & Sherr, 1989; O'Leary, 1981). The partial pressure of CO_2 in seawater (pCO_2, which is strongly controlled by temperature), appears to have a dominant effect on phytoplankton $\delta^{13}C$, with higher ambient pCO_2 associated with a higher degree of discrimination against ${}^{13}C$ and thus a lower $\delta^{13}C_{SPM}$, and vice versa (François et al., 1993; Rau et al., 1989, 1991, 1992).

Phytoplankton $\delta^{15}N$ (often approximated by the $\delta^{15}N$ of SPM; $\delta^{15}N_{SPM}$) is set by the $\delta^{15}N$ of the nitrogenous nutrients supporting growth (e.g., nitrate vs. ammonium; Treibergs et al., 2014), as well as the kinetic isotopic fractionation occurring during N assimilation (e.g., Granger et al., 2004; Needoba et al., 2004). For example, phytoplankton preferentially consume ${}^{14}N$-bearing nitrate, causing the residual pool to become progressively enriched in ${}^{15}N$ as nitrate consumption proceeds (Mariotti et al., 1981; Sigman et al., 1999). In the summertime Southern Ocean, variations in surface $\delta^{15}N_{SPM}$ have been attributed to isotope fractionation during nitrate consumption, with a strong negative correlation observed between surface nitrate concentration and $\delta^{15}N_{SPM}$ (Altabet & Francois, 1994; Lourey et al., 2003; Smart et al., 2020). However, the $\delta^{15}N$ of phytoplankton (and thus SPM) is also influenced by other N nutrients that support production, with the assimilation of recycled N (e.g., ammonium) typically yielding a lower $\delta^{15}N_{SPM}$ than the consumption of nitrate supplied from depth (Altabet, 1988; Fawcett et al., 2011, 2014; Treibergs et al., 2014). Because of the different isotopic signals of nitrate versus ammonium assimilation, $\delta^{15}N_{SPM}$ can be used to distinguish "new" versus "regenerated" N uptake by phytoplankton (e.g., Fawcett et al., 2011, 2014; Lourey et al., 2003; Van Oostende et al., 2017). Moreover, since the rate of new N uptake by phytoplankton must be balanced by the downward flux of organic matter ("export production"), distinguishing nitrate- from ammonium-fueled NPP using $\delta^{15}N_{SPM}$ provides a means of estimating carbon export potential (Dugdale & Goering, 1967; Eppley & Peterson, 1979; Fawcett et al., 2011).

Maps showing the spatial distribution of $\delta^{13}C_{SPM}$ and $\delta^{15}N_{SPM}$ (i.e., "isoscapes") are increasingly used to address large-scale ecological and biogeochemical questions (e.g., Bowen, 2010; Espinasse et al., 2019; St John Glew et al., 2021; West et al., 2009). Such studies have described gradients in $\delta^{13}C_{SPM}$ and $\delta^{15}N_{SPM}$ across the Southern Ocean, with many reporting relatively stable values within hydrographic zones but substantial inter-zone differences (e.g., Espinasse et al., 2019; François et al., 1993; Smith et al., 2022; St John Glew et al., 2021). Recently, St John Glew et al. (2021) used an Integrated Nested LaPlace Approximation-based approach constrained by

measured environmental variables to predict $\delta^{13}C_{SPM}$ and $\delta^{15}N_{SPM}$ for the entire Southern Ocean. The authors found that $\delta^{13}C_{SPM}$ and $\delta^{15}N_{SPM}$ generally decreased southwards, coincident with changes in sea surface temperature (SST) and N nutrient availability. Additionally, $\delta^{13}C_{SPM}$ and $\delta^{15}N_{SPM}$ increased near Antarctica, the (Sub) Antarctic islands, and within the MIZ, as has been observed by others (Espinasse et al., 2019; Smart et al., 2020; Trull et al., 2008). While this meta-analysis represents a significant improvement in Southern Ocean isoscape coverage, particularly for regions where sample collection has been limited, more direct observations are needed to fill sampling gaps and validate isoscape models (St John Glew et al., 2021). In addition, because SPM includes diverse living and dead autotrophic and heterotrophic material, measurements of $\delta^{13}C_{SPM}$ and $\delta^{15}N_{SPM}$ that are not accompanied by phytoplankton assemblage data may yield a limited view of the biogeochemical functioning of a system (Falkowski, 1991). Another shortcoming of $\delta^{15}N_{SPM}$ isoscapes in particular is that they often do not consider variations in the $\delta^{15}N$ of the nitrate supply as a potential driver of $\delta^{15}N_{SPM}$ variability (*cf.* Van Oostende et al., 2017). However, the $\delta^{15}N$ of the nitrate source to surface waters (e.g., Subantarctic Mode Water; SAMW) can change by >2‰ across the Southern Ocean (Fripiat et al., 2021; Rafter et al., 2013), such that for the same amount of nitrate consumption, and without varying any other environmental parameter, phytoplankton biomass $\delta^{15}N$ (and thus, $\delta^{15}N_{SPM}$) could also differ by >2‰.

Here, we present circum-Antarctic $\delta^{13}C_{SPM}$ and $\delta^{15}N_{SPM}$ isoscapes and phytoplankton community composition data collected during the summer 2016/17 Antarctic Circumnavigation Expedition (ACE). The ACE cruise provided a unique opportunity to collect samples across all sectors of the Southern Ocean during a single season. As such, a major advantage of our dataset is its high spatial resolution, which means that very little interpolation is required (Brault et al., 2018). Below, we discuss possible drivers of isotopic variability among and within the Southern Ocean's hydrographic zones and, by applying a two-endmember isotope mixing model to our $\delta^{15}N_{SPM}$ data, constrain phytoplankton reliance on new versus recycled N, from which we can estimate relative summertime carbon export potential.

2. Materials and Methods

2.1. Sample Collection

The ACE cruise occurred during summer 2016/17 aboard the R/V *Akademik Treshnikov* (*Академик Трёшников*) (Landwehr et al., 2021; Walton & Thomas, 2018). The vessel circumnavigated Antarctica in three legs (Figure 1): Leg1 between Cape Town and Hobart (Indian sector; Figure 1b); Leg2 between Hobart and Punta Arenas (Pacific sector; Figure 1c); and Leg3 between Punta Arenas and Cape Town (Atlantic sector; Figure 1d). Leg1 and Leg3 crossed the open Southern Ocean zonally, visiting the Prince Edward Islands (PEIs), Crozet, Kerguelen, and Heard Islands (Leg1), and South Georgia, the South Sandwich, and Bouvet Islands (Leg3). Leg2 followed the Antarctic coastline, sampling the MIZ and visiting the Mertz Glacier and Balleny, Scott, Siple, Peter 1st, and Diego Ramírez Islands.

Seawater samples were collected from the ship's underway system (~4.5 m intake) every one to three hours while the ship was steaming (330 stations) and from Niskin bottles triggered between the surface and 200 m during conductivity-temperature-depth (CTD) hydrocast deployments (34 stations). In total, we collected samples at 142, 132, and 90 stations during Leg1, Leg2, and Leg3, respectively.

At the underway stations, samples for phosphate (PO_4^{3-}), silicic acid (SiO_4^{4-}), nitrate ($NO_3^- + NO_2^-$; hereafter, NO_3^-), and nitrite (NO_2^-) concentrations were collected in sample-rinsed 50 mL Falcon tubes that were immediately frozen at −20°C. Samples for ammonium (NH_4^+) concentrations were collected in 50 mL "aged" high-density polyethylene (HDPE) bottles (Smith et al., 2022) and analyzed on board within 24 hr of collection (Leg2 and Leg3) or frozen and measured on land (Leg1). Nutrient samples were also collected at the CTD stations (Hassler & Ellwood, 2020; Janssen et al., 2020) and iron concentrations were measured for samples collected at 17 CTD stations during Leg1 and Leg2 (Janssen et al., 2020).

To capture the bulk SPM, duplicate 2L seawater aliquots were collected at all the underway and all but two of the CTD stations in sample-rinsed opaque HDPE bottles, then filtered through pre-combusted (450°C for 8 hr) glass fiber filters (GF-75s; 0.3 μm pore size). Filters were stored in pre-combusted foil envelopes at −80°C until analysis.
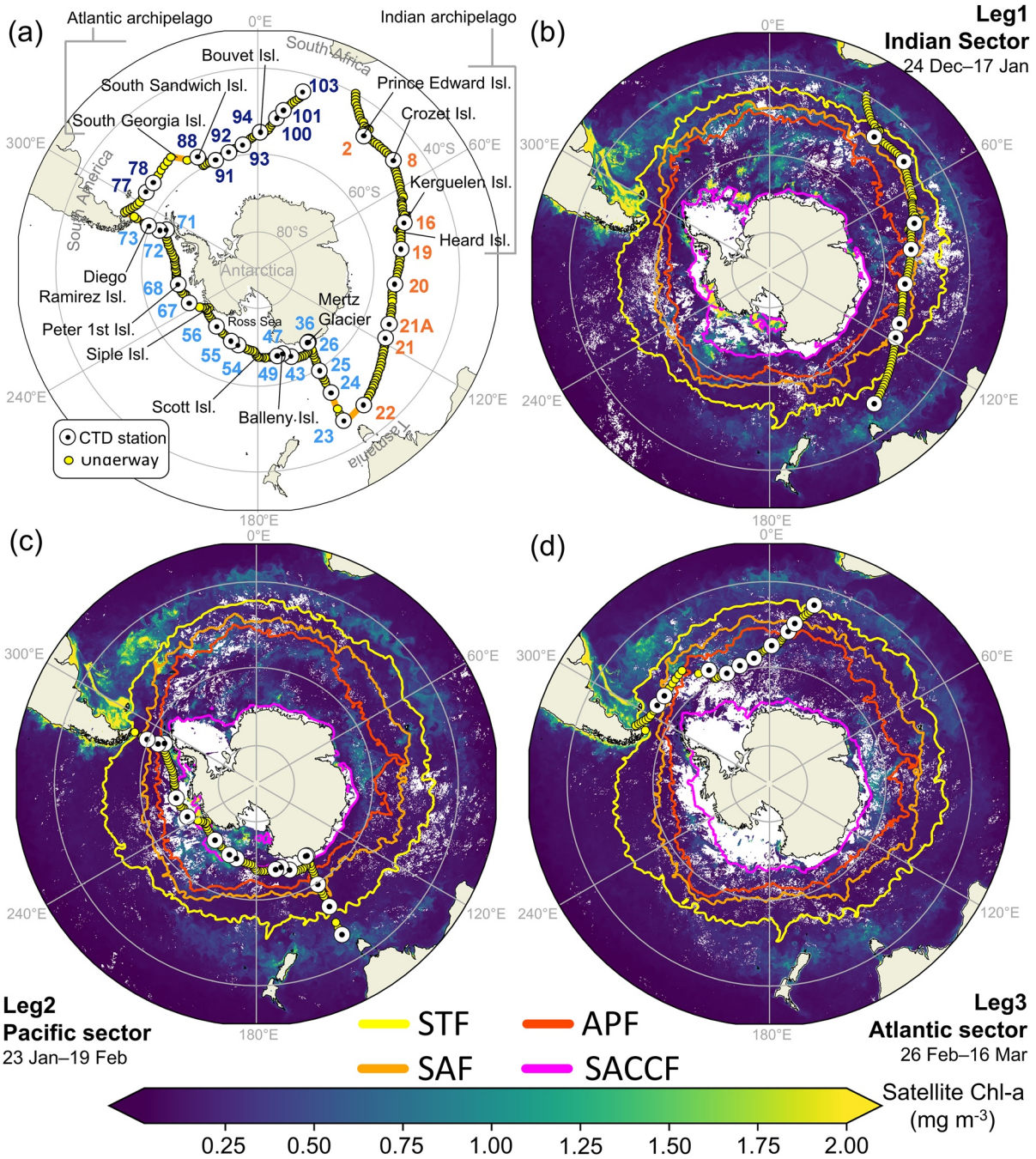
Figure 1. (a) Cruise track and stations sampled during the Antarctic Circumnavigation Expedition. Yellow dots indicate underway stations, white/black dots show conductivity-temperature-depth stations, and numbers are station identifiers, with the font color corresponding to the cruise leg: Leg1 = orange, Leg2 = light blue, Leg3 = dark blue. (b–d) Monthly average satellite-based chlorophyll-*a* concentrations (mg m^{-3}; level-3 Chl-*a* from the Moderate Resolution Imaging Spectroradiometer (MODIS) Aqua satellite product; https://oceandata.sci.gsfc.nasa.gov/MODIS-Aqua/Mapped/Monthly/4km/chlor_a/) at 4 km spatial resolution for each cruise leg overlaid with monthly average frontal positions determined from satellite-derived sea surface temperature (UKMO, 2005) following Orsi et al. (1995) (colored lines: yellow = Subtropical Front (STF), orange = Subantarctic Front (SAF), red = Antarctic Polar Front (APF), purple = Southern Antarctic Circumpolar Current Front (SACCF)).

Samples for micro-phytoplankton (20–200 μm) taxonomy were collected at 83 underway stations. Seawater was filtered through a 20 μm nylon mesh with the volume filtered varying according to the concentration of cells in the water (range of 4.5–60 L). The mesh filters were suspended in 5 mL of 0.2 μm-filtered seawater, fixed via the addition of 5 μL of 25% glutaraldehyde, and stored at 4°C in the dark.

2.2. Sample Analysis

Underway NO_3^- and SiO_4^{4-} concentrations were measured using a Lachat QuickChem flow injection analysis platform (detection limit of 0.5 μM and precision of ≤0.5 μM) (Diamond, 1994; Grasshoff, 1976). PO_4^{3-} and NO_2^- were analyzed manually using standard colorimetric methods (Strickland & Parsons, 1972) and a Thermo Scientific Genesys 30 Visible spectrophotometer (detection limit of 0.05 μM, precision of ≤0.05 μM). Certified reference materials (JAMSTEC) were analyzed during all runs to ensure measurement accuracy. CTD station nutrient samples were analyzed as described by Hassler and Ellwood (2020) and Janssen et al. (2020).

The SPM filters were dried for 24 hr at 40°C, with cored subsamples then packaged into tin capsules that were analyzed for carbon (C) and N content and $\delta^{13}C$ and $\delta^{15}N$ using a Flash 2000 elemental analyzer coupled to a Delta V Plus isotope ratio mass spectrometer (IRMS) (detection limit of 2 μg C and 1 μg N, precision of ±0.2‰ for $\delta^{13}C$ and $\delta^{15}N$). Three in-house standards calibrated against certified reference materials were included in each IRMS run along with numerous blanks (unused pre-combusted filter + tin capsule). Particulate organic C and N (POC and PON) concentrations were calculated by normalizing C and N content to seawater volume filtered. The station-specific $\delta^{13}C_{SPM}$ and $\delta^{15}N_{SPM}$ reported hereafter are the POC- and PON concentration-weighted averages of duplicate samples.

Phytoplankton taxonomic identification involved gently homogenizing each preserved sample, then transferring 0.08 mL onto two clean microscope slides. Cells with intact chloroplasts (i.e., alive at the time of sampling) were counted at 630× magnification using a Zeiss Axioscope A1 light microscope; all live cells on both slides were counted. The remaining volume of preserved sample was treated with 10% hydrochloric acid and 37% hydrogen peroxide to remove carbonate particles and organic matter, respectively. Permanent slides were prepared by pipetting distilled-water-cleaned material onto acid-washed coverslips that were air-dried overnight, then mounted onto glass slides using Naphrax® mountant (refractive index of 1.7). The permanent slides were examined using a Zeiss Axioscope A1 light microscope equipped with differential interference contrast at 1,000× magnification under oil immersion. Stubs were also prepared from the cleaned material for examination using a JEOL JSM-7001F field emission scanning electron microscope to visualize the morphological features not evident under the light microscope.

2.3. Supporting Data Products

Satellite data were used to supplement the ship-based surface hydrography measurements (Text S1 in Supporting Information S1). Daily high-resolution SST (GHRSST) Level-4 data on a global 0.054° grid from the Operational Sea Surface Temperature and Ice Analysis database (https://podaac.jpl.nasa.gov/dataset/UKMO-L4HRfnd-GLOB-OSTIA; UKMO, 2005) were used to determine the positions of the major oceanic fronts following Orsi et al. (1995): The Subtropical Zone (STZ) north of the Subtropical Front (STF) is characterized by an SST of 20°C–10°C. Between the STF and Subantarctic Front (SAF) is the Subantarctic Zone (SAZ) with an SST of 10°C–6°C, while the Polar Frontal Zone (PFZ) between the SAF and Antarctic Polar Front (APF) has an SST of 6°C–4°C. The PFZ is characterized by high physical variability and is often considered the transition zone between Antarctic and Subantarctic waters (Bowie et al., 2011; Orsi et al., 1995); here, we take the APF as the boundary between these two major regions. South of the APF is the Southern Antarctic Circumpolar Current Zone (SACCZ), which remains ice-free year-round. The SACCZ has an SST of 4°C–0.7°C and is bounded to the south by the Southern ACC Front (SACCF), the southern edge of the ACC core (Orsi et al., 1995). South of the SACCF is the southern Boundary Zone (sBZ), which experiences seasonal sea-ice cover (Squire, 2022). We group all stations south of the SACCF, including in the Antarctic Continental Zone, into the sBZ.

Monthly level-3 chlorophyll-*a* (Chl-*a*) concentrations from the MODIS Aqua satellite product (https://oceandata.sci.gsfc.nasa.gov/MODIS-Aqua/Mapped/Monthly/4km/chlor_a/) at 4 km spatial resolution were used to visualize the large-scale phytoplankton biomass distributions (Figures 1b–1d). We used the monthly average data product from January 2017 for Leg1, February 2017 for Leg2, and March 2017 for Leg3. In addition, phytoplankton pigment samples were collected underway every three hours and analyzed using High Performance Liquid Chromatography (HPLC) (Antoine et al., 2020). We used the HPLC total Chl-*a* concentration (the sum of monovinyl Chl-*a*, divinyl Chl-*a*, chlorophyllide *a*, and Chl-*a* allomers and epimers) as a measure of phytoplankton biomass. Seven marker pigments were weighted as per Uitz et al. (2006) and used to estimate the percent contribution of different phytoplankton size classes to Chl-*a* (i.e., pico- (0–2 μm), nano- (2–20 μm), and micro-phytoplankton

(20–200 μm); Vidussi et al., 2001). We also quantified the Chl-*a* biomass contributed by 10 different taxonomic groups using the CHEMTAX v1.95 chemical taxonomy software (Mackey et al., 1996).

Surface ocean pCO_2 (Pa), air-sea CO_2 flux (fCO_2; mg m^{-2} h^{-1}), and pH were obtained from a monthly 1-degree resolution global reconstructed product (resources.marine.copernicus.eu/product-detail/MULTIOBS_GLO_BIO_CARBON_SURFACE_REP_015_008) that was created by interpolation using an ensemble of artificial neural networks (https://doi.org/10.48670/moi-00047). We used the monthly average data product from January 2017 for Leg1, February 2017 for Leg2, and March 2017 for Leg3.

2.4. An Isotopic Framework for Assessing Phytoplankton Dependence on Nitrate Versus Ammonium

Since $\delta^{15}N_{SPM}$ is strongly influenced by the N nutrients consumed by phytoplankton (e.g., Fawcett et al., 2011; Lourey et al., 2003) and given that phytoplankton reliance on new N is quantitatively related to export production (Dugdale & Goering, 1967; Eppley & Peterson, 1979), our SPM data can be used to estimate relative carbon export potential across the summertime Southern Ocean.

While the 0.3 μm filters likely trapped some non-phytoplankton material, including bacteria, we assume that the surface SPM was dominated by actively growing phytoplankton (e.g., Popp et al., 1999; Trull & Armand, 2001), a notion supported by the measured POC:PON ratios (Section 3.2). As such, $\delta^{15}N_{SPM}$ can be described by a two-endmember isotope mixing model (Fawcett et al., 2011) as:

$$\delta^{15}N_{SPM} = \delta^{15}N_{SPM_{new}} \times f_{new} + \delta^{15}N_{SPM_{RN}} \times f_{RN} \tag{1}$$

where $\delta^{15}N_{SPM_{new}}$ and $\delta^{15}N_{SPM_{RN}}$ are the $\delta^{15}N$ values of phytoplankton biomass produced from the assimilation of new and regenerated N, respectively, and f_{new} and f_{RN} are the fraction of phytoplankton growth fueled by new and regenerated N (with $f_{new} + f_{RN} = 1$). The fraction of new production can thus be computed as:

$$f_{new} = \frac{(\delta^{15}N_{SPM} - \delta^{15}N_{SPM_{RN}})}{\left(\delta^{15}N_{SPM_{new}} - \delta^{15}N_{SPM_{RN}}\right)} \tag{2}$$

We assume that regenerated N is well represented by NH_4^+, which is dominantly sourced in the surface layer from SPM remineralization. We did not directly measure $\delta^{15}N_{NH_4^+}$ because it is currently near-impossible to analyze at the low NH_4^+ concentrations characteristic of the open ocean (L. Zhang et al., 2007). However, $\delta^{15}N_{NH_4^+}$ should be low given the isotope effects associated with its production (Checkley & Miller, 1989; Macko et al., 1986; Möbius, 2013; Silfer et al., 1992), its short residence time in the surface layer in summer (days; Smith et al., 2022), and the fact that the flux of low-$\delta^{15}N$ remineralized NH_4^+ should be fairly high (Smith et al., 2022). We estimate $\delta^{15}N_{NH_4^+}$ as:

$$\delta^{15}N_{NH_4^+} = \delta^{15}N_{SPM} - \varepsilon_{regen} \tag{3}$$

where ε_{regen} is the isotope effect associated with NH_4^+ regeneration, set here to 1.5‰. While ε_{regen} has been estimated under steady state conditions to be ~3‰ (Möbius, 2013), we use a lower value because (a) processes other than regeneration are coincidentally acting on the SPM, violating the steady state assumption and altering $\delta^{15}N_{SPM}$; (b) while the primary fate of regenerated NH_4^+ is consumption by phytoplankton, some NH_4^+ will have accumulated over a variable time period and as such, is unlikely to have a $\delta^{15}N$ equal to that of the NH_4^+ instantaneously produced from the in situ SPM; and (c) previous studies of SPM and our own preliminary measurements of $\delta^{15}N_{NH_4^+}$ from elsewhere in the Southern Ocean indicate that it averages −1‰ in summer (Flynn, 2023). We compute a mean $\delta^{15}N_{NH_4^+}$ using Equation 3 of −0.99 ± 0.13‰. In the open ocean where NH_4^+ concentrations are <<5 μM, NH_4^+ assimilation is thought to occur with little to no isotopic fractionation (Hoch et al., 1992; Liu et al., 2013; Pennock et al., 1996); thus, $\delta^{15}N_{SPM_{RN}} = \delta^{15}N_{NH_4^+}$.

Determining $\delta^{15}N_{SPM_{new}}$ is more complex because NO_3^- is never fully consumed in Southern Ocean surface waters and it is fractionated during assimilation (Granger et al., 2004; Mariotti et al., 1981). The effect of this fractionation can be characterized using the Rayleigh model, which describes a unidirectional reaction (i.e., NO_3^- assimilation into SPM) that proceeds with a constant isotope effect (ε_{assim}) under conditions where the reactant NO_3^- is neither resupplied (e.g., by mixing) nor lost by any mechanism other than phytoplankton assimilation

(Mariotti et al., 1981). In the Southern Ocean in summer, the N isotope dynamics of NO_3^- assimilation are reasonably well described by the Rayleigh model since NO_3^- is supplied to the surface mainly during winter mixing, then assimilated in spring and summer following surface-layer stratification (Sigman et al., 1999).

The Rayleigh model describes the isotopic evolution of the reactant pool ($\delta^{15}N_{reactant}$; Equation 4a), the instantaneously generated product pool ($\delta^{15}N_{instantaneous}$; Equation 4b), and the accumulated product pool ($\delta^{15}N_{accumulated}$; Equation 4c) (Mariotti et al., 1981) as:

$$\delta^{15}N_{reactant} = \delta^{15}N_{source} - \varepsilon_{assim} \times \ln(F) \tag{4a}$$

$$\delta^{15}N_{instantaneous} = \delta^{15}N_{reactant} - \varepsilon_{assim} \tag{4b}$$

$$\delta^{15}N_{accumulated} = \delta^{15}N_{source} + \varepsilon_{assim} \times \left\{ \frac{F \times \ln(F)}{(1-F)} \right\} \tag{4c}$$

where $\delta^{15}N_{source}$ is the initial $\delta^{15}N$ of the NO_3^- supplied to surface waters in winter and F is the fraction of this NO_3^- remaining at the time of sampling (i.e., the measured surface NO_3^- concentration ($[NO_3^-]_{meas}$) divided by the source NO_3^- concentration ($[NO_3^-]_{source}$)). The $\delta^{15}N_{instantaneous}$ is the SPM produced from NO_3^- at each moment of its consumption, while the $\delta^{15}N_{accumulated}$ is the sum of all the SPM produced from NO_3^- since consumption began (Mariotti et al., 1981). While some phytoplankton biomass accumulates in surface waters during the growth season (e.g., Swart et al., 2015; van Leeuwe et al., 2020), a significant fraction will also be exported (indeed, we estimate that $60 \pm 40\%$ of the SPM produced since the start of the growth season was exported prior to our sampling; Text S2 in Supporting Information S1). As such, neither $\delta^{15}N_{accumulated}$ nor $\delta^{15}N_{instantaneous}$ can reliably approximate the $\delta^{15}N$ of SPM generated from NO_3^- assimilation (i.e., $\delta^{15}N_{SPM_{new}}$).

We propose that $\delta^{15}N_{SPM_{new}}$ can instead be estimated by summing the $\delta^{15}N_{instantaneous}$ over the concentration of $SPM + NH_4^+$ measured in the surface layer at the time of sampling, since this $SPM + NH_4^+$ represents the product of $NO_3^-_{source}$ consumption that has not been exported. As such, Equation 4a can be modified as:

$$\delta^{15}N_{reactant\_sampling} = \delta^{15}N_{source} - \varepsilon_{assim} \times \ln \frac{\left([NO_3^-] + SPM + [NH_4^+]\right)_{meas}}{[NO_3^-]_{source}} \tag{5}$$

where $\delta^{15}N_{reactant\_sampling}$ is the theoretical $\delta^{15}N$ of surface NO_3^- at the concentration of total measured N (i.e., $([NO_3^-] + [SPM] + [NH_4^+])_{meas}$) present in the surface layer at the time of sampling. Using Equation 4c, but summing over only the measured surface-layer $SPM + NH_4^+$, we compute $\delta^{15}N_{SPM_{new}}$ as:

$$\delta^{15}N_{SPM_{new}} = \delta^{15}N_{reactant\_sampling} + \varepsilon_{assim} \times \frac{F_{meas} \times \ln(F_{meas})}{1 - F_{meas}} \tag{6}$$

Here, F_{meas} is the fraction of $NO_3^-_{source}$ remaining in the surface layer at the time of sampling (i.e., both as NO_3^- and as SPM and NH_4^+ ultimately derived from $NO_3^-_{source}$), after accounting for the amount of the source NO_3^- that was consumed by phytoplankton and exported from the surface layer earlier in the growth season (Text S2 in Supporting Information S1):

$$F_{meas} = \frac{[NO_3^-]_{meas}}{\left([NO_3^-] + SPM + [NH_4^+]\right)_{meas}} \tag{7}$$

We note that if $\delta^{15}N_{SPM_{new}}$ is approximated by either the instantaneous or the accumulated product equations (Equations 4b and 4c), our definition of $\delta^{15}N_{SPM_{new}}$ (Equation 6) will still return the correct value of $\delta^{15}N_{instantaneous}$ or $\delta^{15}N_{accumulated}$ (Figure S2 in Supporting Information S1).

In applying Equation 6 to our dataset, we assume that $NO_3^-_{source}$ is the NO_3^- that was present in the mixed layer directly following winter convection, which can be approximated by the NO_3^- measured between the base of the summer mixed layer and the maximum depth of the winter mixed layer; we refer to the waters between the winter and summer mixed layer depths (MLDs) as W-S. We use the biogeochemical-Southern Ocean State Estimate (Mazloff et al., 2010; Verdy & Mazloff, 2017) to estimate the concentration of $NO_3^-_{W-S}$ and the neural-network-based global ocean NO_3^- $\delta^{15}N$ database of Rafter et al. (2019) to estimate $\delta^{15}N_{NO_3^-(W-S)}$ (Texts S3 and S4 in Supporting Information S1). For stations near islands and continents (117 in total), we used the average NO_3^-

Table 1
Medians (±IQR) of the Sea Surface Temperature (SST; °C), Concentrations of Nitrate (NO$_3^-$; μM), Phosphate (PO$_4^{3-}$; μM), Silicic Acid (SiO$_4^{4-}$; μM), and Ammonium (NH$_4^+$; μM), the Partial Pressure of CO$_2$ (pCO$_2$; Pa), and the Air-Sea Flux of CO$_2$ (fCO$_2$; mg m^{-2} h^{-1}) Measured During ACE: "Subantarctic" Includes the STZ = Subtropical Zone, SAZ = Subantarctic Zone, and PFZ = Polar Frontal Zone, While "Antarctic" Includes the SACCZ = Southern Antarctic Circumpolar Current Zone and sBZ = Southern Boundary Zone

Region	SST (°C)	NO$_3^-$ (μM)	PO$_4^{3-}$ (μM)	SiO$_4^{4-}$ (μM)	NH$_4^+$ (μM)	pCO$_2$ (Pa)	fCO$_2$ (mg m^{-2} h^{-1})
Subantarctic	6.62 ± 3.44 (196)	20.29 ± 7.43 (177)	1.46 ± 0.39 (177)	2.64 ± 6.91 (177)	0.81 ± 0.65 (196)	38.80 ± 1.42 (196)	1.26 ± 1.54 (196)
Antarctic	1.86 ± 1.58 (166)	23.37 ± 3.68 (142)	1.56 ± 0.26 (142)	40.62 ± 21.05 (142)	0.88 ± 0.66 (166)	36.88 ± 2.84 (166)	2.23 ± 1.94 (166)
STZ	11.89 ± 2.25 (38)	8.37 ± 5.26 (35)	0.72 ± 0.44 (35)	1.04 ± 0.42 (35)	0.63 ± 0.39 (38)	37.03 ± 2.52 (38)	3.54 ± 3.30 (38)
SAZ	7.31 ± 1.44 (77)	19.92 ± 3.52 (71)	1.46 ± 0.24 (71)	2.31 ± 2.79 (71)	0.98 ± 0.62 (77)	39.02 ± 0.29 (77)	1.10 ± 0.62 (77)
PFZ	5.01 ± 0.72 (81)	23.37 ± 3.72 (71)	1.53 ± 0.20 (71)	9.30 ± 7.40 (71)	0.72 ± 1.20 (81)	38.66 ± 1.60 (81)	1.33 ± 1.75 (81)
SACCZ	2.28 ± 1.37 (141)	23.15 ± 3.50 (122)	1.56 ± 0.23 (122)	39.03 ± 23.04 (122)	0.94 ± 0.61 (141)	37.08 ± 2.07 (141)	2.08 ± 1.70 (141)
sBZ	0.45 ± 0.27 (25)	24.29 ± 4.46 (20)	1.56 ± 0.42 (20)	46.26 ± 11.28 (20)	0.42 ± 0.34 (25)	33.98 ± 7.68 (25)	3.76 ± 4.47 (25)

Note. In parentheses are the numbers of observations used to calculate the medians ±IQRs.

concentration and δ^{15}N from 200 to 300 m to represent the source NO$_3^-$ ([NO$_3^-$]$_{(200-300)}$ and δ^{15}N$_{NO_3^-(200-300)}$, respectively) as land-adjacent waters are influenced by physical processes that can supply NO$_3^-$ from below the winter mixed layer (e.g., topographic upwelling, internal waves; De Falco et al., 2022).

While estimates of ε_{assim} for the summertime Southern Ocean have been observed to vary considerably (DiFiore et al., 2010; Fripiat et al., 2019; Karsh et al., 2003; Lourey et al., 2003; Sigman et al., 1999), DiFiore et al. (2010) showed a strong linear correlation between the summer MLD and ε_{assim} (Equation 8). We use this relationship to derive ε_{assim} at each station before calculating a median ε_{assim} for each hydrographic zone:

$$\varepsilon_{assim} = 0.07 \times MLD_{summer} + 4\%_0 \tag{8}$$

Via the approach outlined above, we can estimate δ^{15}N$_{SPM_{RN}}$ and δ^{15}N$_{SPM_{new}}$, which we then incorporate into Equation 2 to estimate f_{new} from our SPM data.

2.5. Statistical Analyses

We used R for statistical analysis of our data (R Core Team, 2018) and Python (van Rossum, 1995) and Ocean Data View (Schlitzer, 2021) for data visualization. Results are reported as mean ± 1 standard deviation, median$_{Q1}^{Q3}$, where Q_1 = first quartile and Q_3 = third quartile, or median ± interquartile range (IQR), where IQR = $Q_3 - Q_1$.

Shapiro-Wilk tests, quantile-quantile plot analysis, and Levene's tests were performed to assess the normality and homogeneity of variance of data distributions. Data were sub-grouped according to geographical region (hydrographic zones = STZ, SAZ, PFZ, SACCZ, and sBZ; oceans = Subantarctic and Antarctic). While parametric assumptions were satisfied when data were grouped as Subantarctic or Antarctic, the equal variance assumption was violated when data were sub-grouped into the five hydrographic zones. Non-parametric analyses were thus used to test for differences among zones. Parametric analyses included analysis of variance and t-tests, while non-parametric analyses included the Kruskal-Wallis test and multiple pairwise-Wilcoxon test. When multiple statistical tests were performed on a single dataset, the probability values were adjusted using the Bonferroni correction (Chen et al., 2017). Hereafter, the probability values obtained from the parametric and non-parametric tests are denoted as p-value(s) and p-value(s)*, respectively.

The *lm R*-function was used for linear regression model analysis of the surface SPM data, with the p-value and R^2 reported for each model. When the assumption of equal variance was violated, we applied a weighted least squares model and report the p-value$_{WLS}$ and R^2_{WLS}. Spearman's rank correlation (ρ) was used as a non-parametric measure of how well the relationship between two variables was described by a monotonic function. A Principal Component Analysis (PCA) was performed to investigate how various parameters (e.g., SST, nutrient concentrations, δ^{15}N$_{SPM}$) influenced data variance and distribution, with clustering based on observational similarity. Biodiversity and evenness were determined for the taxonomic counts using the Shannon-Wiener index (H').

3. Results

3.1. Oceanic Setting

The satellite Chl-*a* concentrations and positions of the major oceanic fronts at the time of sampling are shown in Figures 1b–1d. The surface distributions of the main contextual parameters (i.e., NO$_3^-$, PO$_4^{3-}$, SiO$_4^{4-}$, NH$_4^+$, iron, pCO$_2$) are presented in Table 1 and Figure 2.
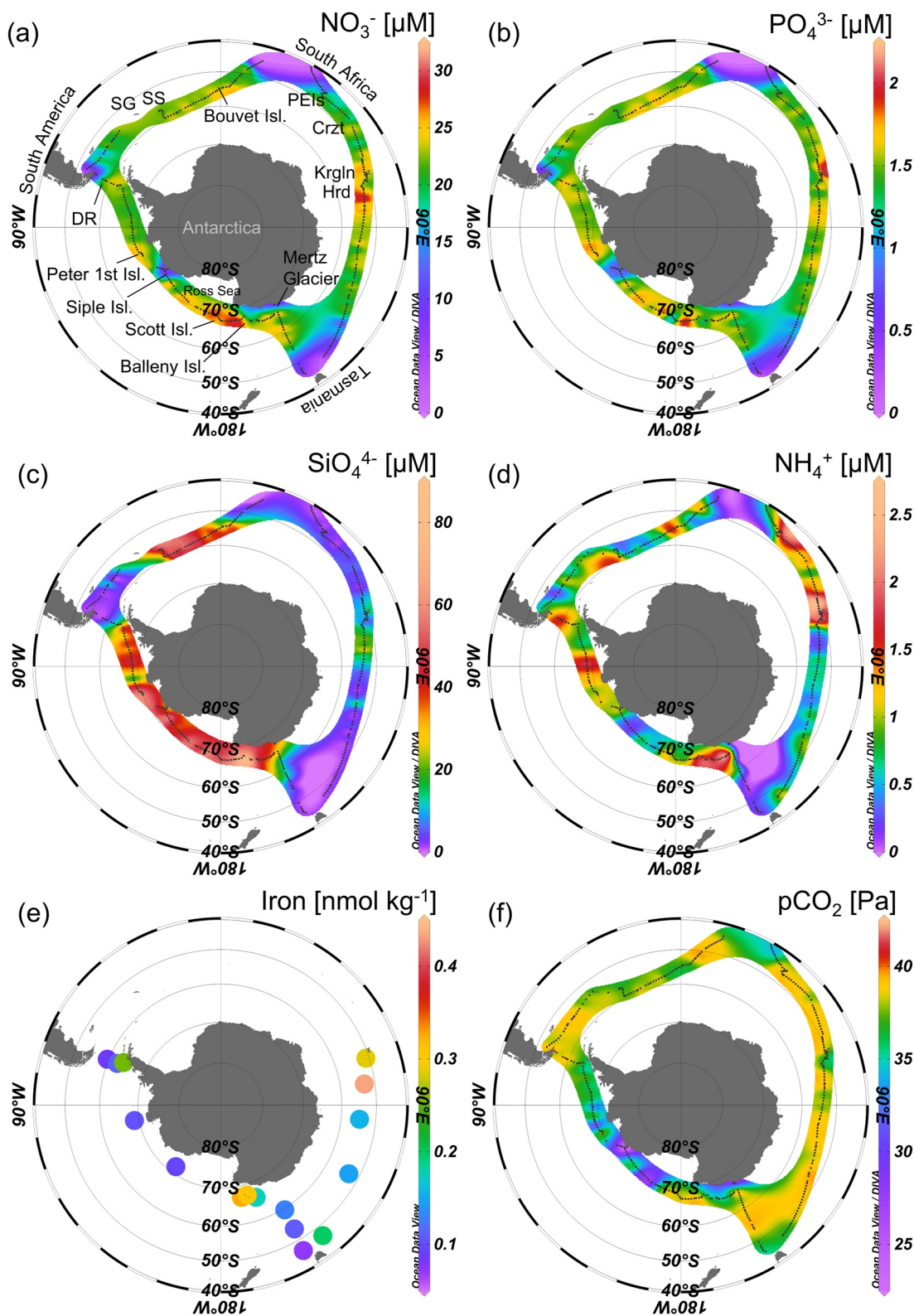
Figure 2. Surface distributions of the (a) nitrate (NO_3^-; μM), (b) phosphate (PO_4^{3-}; μM), (c) silicic acid (SiO_4^{4-}; μM), (d) ammonium (NH_4^+; μM), and (e) iron (nmol kg^{-1}) concentrations, and (f) the partial pressure of CO_2 (pCO_2; Pa) measured during the Antarctic Circumnavigation Expedition. The islands visited during the cruise are indicated on panel (a): PEIs = Prince Edward Islands, Crzt = Crozet Island, Krgln = Kerguelen Island, Hrd = Heard Island, DR = Diego Ramírez Island, SG = South Georgia, and SS = South Sandwich Islands.

Surface NO_3^- and PO_4^{3-} concentrations and pCO_2 increased from the STZ to the SAF (from $8.37_{6.18}^{11.43}$ to $19.92_{17.82}^{21.70}$ µM, from $0.72_{0.56}^{1.32}$ to $1.46_{1.32}^{1.56}$ µM, and from $37.0_{35.9}^{38.4}$ to $39.0_{38.8}^{39.1}$ Pa, respectively; p-values* <0.001; Figures 2a, b, and f) while the air-sea flux of CO_2 (fCO_2) decreased (from $3.54_{1.63}^{4.93}$ to $1.10_{0.75}^{1.37}$ mg m^{-2} h^{-1}; p-value* <0.001; Table 1 and Figure S5 in Supporting Information S1). South of the SAF, the NO_3^- and PO_4^{3-} concentrations remained constant toward Antarctica ($23.40_{21.2}^{24.9}$ and $1.56_{1.43}^{1.66}$ µM; p-values* = 1). pCO_2 also changed minimally until ∼65°S ($38.6_{37.2}^{39.0}$ Pa), south of which it decreased strongly, with minimum values at the mouth of the Ross Sea and near Siple Island (∼23.0 Pa). Flux of CO_2 was highly variable in the PFZ (∼0–5.59 mg m^{-2} h^{-1}), becoming more constant south of the APF to ∼65°S ($1.82_{0.83}^{2.39}$ mg m^{-2} h^{-1}), then increasing toward Antarctica to reach a maximum where pCO_2 was lowest (>10 mg m^{-2} h^{-1}). The near-island waters hosted elevated surface NO_3^- and PO_4^{3-} concentrations, particularly over the Indian archipelago (formed by the PEIs, Crozet and Kerguelen Islands), the Balleny Islands, and Peter 1st Island (>25 µM and >1.8 µM, respectively). Waters near the Atlantic archipelago (formed by South Georgia, South Sandwich, and Bouvet Islands) also hosted elevated NO_3^- and PO_4^{3-}, although their surface concentrations were lower than at the Indian sector islands (20–25 µM and 1.3–1.8 µM, respectively). Surface pCO_2 was lower near the islands than in the surrounding offshore waters (<36 Pa), while fCO_2 was higher (>2.5 mg C m^{-2} h^{-1}).

The surface SiO_4^{4-} concentrations increased gradually from the STZ to the APF ($1.04_{0.92}^{1.34}$ µM to $9.30_{4.39}^{11.8}$ µM) before increasing sharply southwards (Antarctic = $40.60_{38.50}^{51.50}$ µM) to reach ∼80 µM near the Balleny Islands (Figure 2c). The SiO_4^{4-} concentrations over the Atlantic archipelago were higher than elsewhere on Leg3 because this region is located in the SACCZ. In the Subantarctic, SiO_4^{4-} was highest downstream of Kerguelen Island (>15 µM).

The surface NH_4^+ concentrations were variable along the transect, ranging from lower values in the open ocean ($0.72_{0.50}^{1.02}$ µM) to higher concentrations near the islands ($1.17_{0.73}^{1.73}$ µM). NH_4^+ concentrations near Peter 1st, Diego Ramírez, South Sandwich, and Bouvet Islands exceeded 1.5 µM, while maximum concentrations of 2.7 µM were measured over the Indian archipelago and near the Balleny Islands (Figure 2d).

Surface dissolved iron concentrations were higher in the eastern Indian sector (second half of Leg1; 0.14–0.43 nmol kg^{-1}) than on Leg2 (0.21–0.33 nmol kg^{-1}), with maxima at Kerguelen Island (0.28 nmol kg^{-1}), downstream of Heard Island (0.43 nmol kg^{-1}), at the Balleny Islands (0.31 nmol kg^{-1}) and the West Antarctic Peninsula (WAP; 0.25 nmol kg^{-1}) (Figure 2e; Janssen et al., 2020). No iron data are available for the first half of Leg1 or Leg3.

3.2. POC and PON Concentrations

The POC and PON concentrations showed similar trends along the transect, ranging from 1.9 to 70.7 µM ($7.4_{5.8}^{9.9}$ µM) and from 0.3 to 7.7 µM ($1.0_{0.8}^{1.4}$ µM), respectively (Figures 3a and 3b). Variable concentrations were measured in the STZ (medians of $10.7_{4.0}^{11.0}$ µM and $1.3_{1.0}^{1.7}$ µM, respectively) and the sBZ (medians of $11.4_{9.2}^{19.2}$ µM and $1.5_{1.3}^{2.2}$ µM, respectively), and these values were significantly higher than those measured in the other zones (p-values* <0.01; Table 2). The POC and PON concentrations in the SAZ, PFZ, and SACCZ were statistically homogeneous (medians of $7.2_{5.6}^{8.9}$ µM and $1.0_{0.8}^{1.2}$ µM, respectively; p-values* = 1.0). Particularly high POC and PON concentrations were measured in the open STZ south of South Africa and in the sBZ near Siple Island (30.0–70.7 µM and 4.0–7.7 µM, respectively), with elevated concentrations also observed near Kerguelen and Bouvet Islands, the Mertz Glacier, the mouth of the Ross Sea, the WAP, and off South America. The POC:PON ratio ranged from 3.5 to 25.1 (median of $7.2_{6.7}^{7.8}$; Figure 3c), with median ratios in the Subantarctic ($7.4_{6.8}^{8.0}$) that were significant different from those in the Antarctic ($6.9_{6.5}^{7.4}$; p-value <0.01).

3.3. POC and PON Isoscapes

For the entire transect, $\delta^{13}C_{SPM}$ and $\delta^{15}N_{SPM}$ ranged from −33.7‰ to −19.6‰ ($-26.6_{-28.4}^{-25.1}$‰) and −5.9–14.4‰ ($0.2_{-1.1}^{+1.7}$‰), respectively (Figures 3d and 3e). Local maxima were apparent in the STZ and near the Indian archipelago, South America, and Siple Island ($\delta^{13}C_{SPM} > -22.0$‰ and $\delta^{15}N_{SPM} > 5.0$‰). Elsewhere, a negative relationship was observed between $\delta^{13}C_{SPM}$ and $\delta^{15}N_{SPM}$. For example, $\delta^{15}N_{SPM}$ at the mouth of the Ross Sea ($0.6_{0.2}^{1.8}$‰) and near the Atlantic archipelago ($1.5_{0.4}^{1.9}$‰) was higher than at the surrounding stations ($-0.8_{-1.8}^{+0.6}$‰ and $0.5_{-1.5}^{+1.8}$‰ for Leg2 and Leg3, respectively), while $\delta^{13}C_{SPM}$ was lower ($-27.6_{-28.4}^{-26.2}$‰ and $-29.9_{-31.0}^{-29.1}$‰ vs. $-28.4_{-28.9}^{-27.5}$‰ and $-25.7_{-26.4}^{-24.8}$‰). Below, we describe the broad latitudinal trends in $\delta^{13}C_{SPM}$ and $\delta^{15}N_{SPM}$, while the longitudinal patterns are shown in Text S5 in Supporting Information S1.
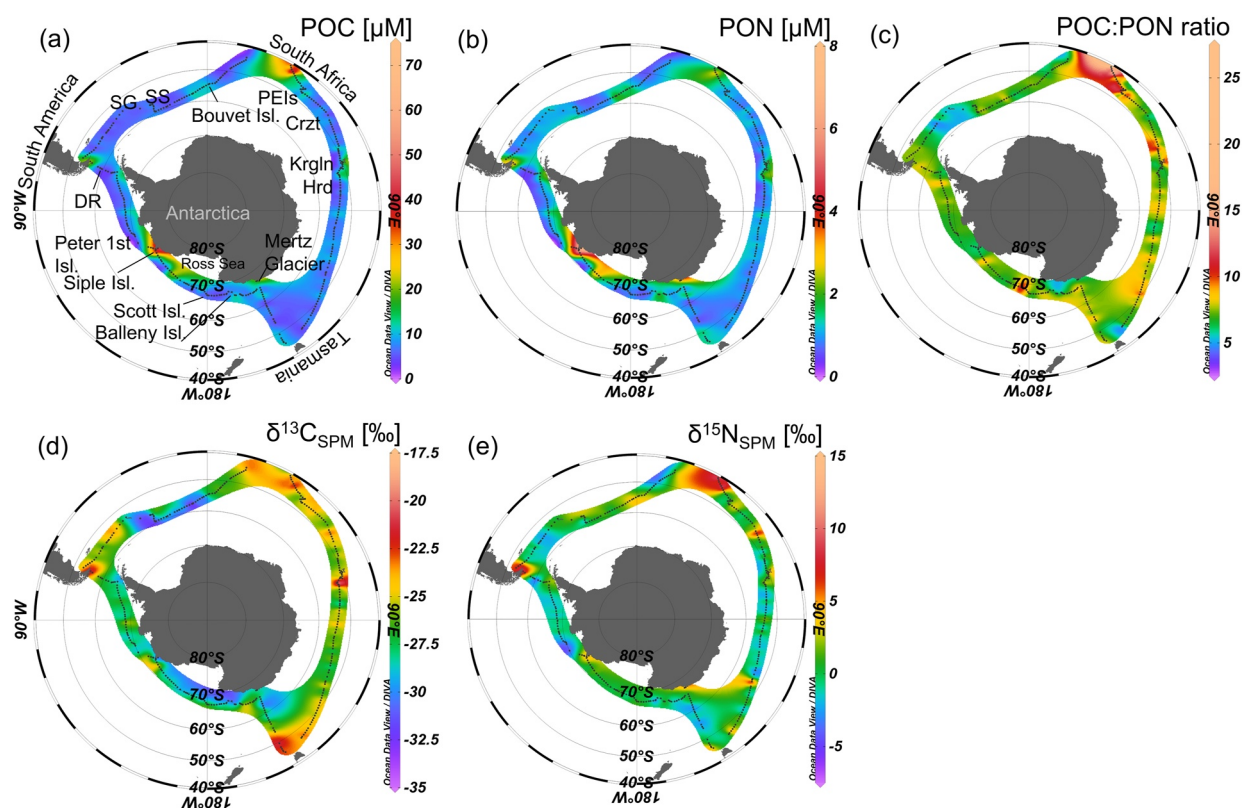
Figure 3. Surface concentrations (μM) of particulate organic (a) carbon (POC) and (b) nitrogen (PON), (c) surface POC:PON ratios, and (d) surface $\delta^{13}C_{SPM}$ (‰) and (e) $\delta^{15}N_{SPM}$ (‰) for samples collected during the Antarctic Circumnavigation Expedition. The islands visited during the cruise are indicated on panel (a): PEIs = Prince Edward Islands, Crzt = Crozet Island, Krgln = Kerguelen Island, Hrd = Heard Island, DR = Diego Ramírez Island, SG = South Georgia, and SS = South Sandwich Islands.

In general, $\delta^{13}C_{SPM}$ decreased with increasing latitude and was higher in the Subantarctic (-25.2 ± 1.9‰, mean $\pm$ 1SD) than the Antarctic (-28.4 ± 1.7‰; p-values <0.001; Table 2, Figure 4a). The boundary between the two regions (~55°S to 60°S) was characterized by a $\delta^{13}C_{SPM}$ minimum (reaching -33.7‰, average of -28.9 ± 2.5‰). While $\delta^{15}N_{SPM}$ was high at many STZ stations (>5‰), the median Subantarctic $\delta^{15}N_{SPM}$ was statistically similar to the median Antarctic $\delta^{15}N_{SPM}$ ($-0.1^{+1.9}_{-1.2}$‰ and $+0.4^{+1.6}_{-1.0}$‰, respectively; p-value* = 0.63; Figure 4b).

Table 2
Medians (±IQR) of the Surface Particulate Organic Carbon (POC) and Nitrogen (PON) Concentrations (μM), POC:PON Ratios, and $\delta^{13}C_{SPM}$ and $\delta^{15}N_{SPM}$ (‰) for the Different Regions of the Southern Ocean Sampled During ACE: "Subantarctic" Includes the STZ = Subtropical Zone, SAZ = Subantarctic Zone, PFZ = Polar Frontal Zone, While "Antarctic" Includes the SACCZ = Southern Antarctic Circumpolar Current Zone and sBZ = Southern Boundary Zone

Region	POC (μM)	PON (μM)	POC:PON ratio	$\delta^{13}C_{SPM}$ (‰)	$\delta^{15}N_{SPM}$ (‰)
Subantarctic	7.3 ± 3.6 (195)	1.0 ± 0.5 (195)	7.4 ± 1.2 (195)	−25.2 ± 2.1 (194)	−0.1 ± 3.1 (194)
Antarctic	7.5 ± 4.9 (166)	1.1 ± 0.7 (166)	6.9 ± 0.9 (166)	−28.4 ± 2.0 (166)	0.4 ± 2.6 (166)
STZ	10.7 ± 7.7 (37)	1.3 ± 0.7 (37)	7.4 ± 1.0 (37)	−23.6 ± 2.3 (37)	2.1 ± 5.4 (37)
SAZ	6.8 ± 2.3 (77)	0.9 ± 0.3 (77)	7.6 ± 1.2 (77)	−25.4 ± 1.3 (76)	−0.1 ± 3.1 (76)
PFZ	7.4 ± 3.3 (81)	1.1 ± 0.5 (81)	7.2 ± 1.3 (81)	−26.1 ± 2.2 (81)	−0.8 ± 2.2 (81)
SACCZ	7.1 ± 3.8 (141)	1.0 ± 0.5 (141)	6.9 ± 0.9 (141)	−28.4 ± 2.2 (141)	0.3 ± 2.8 (141)
sBZ	11.4 ± 10.0 (25)	1.5 ± 0.9 (25)	6.8 ± 0.9 (25)	−28.4 ± 0.8 (25)	0.6 ± 1.3 (25)

Note. In parentheses are the numbers of observations used to calculate the medians.
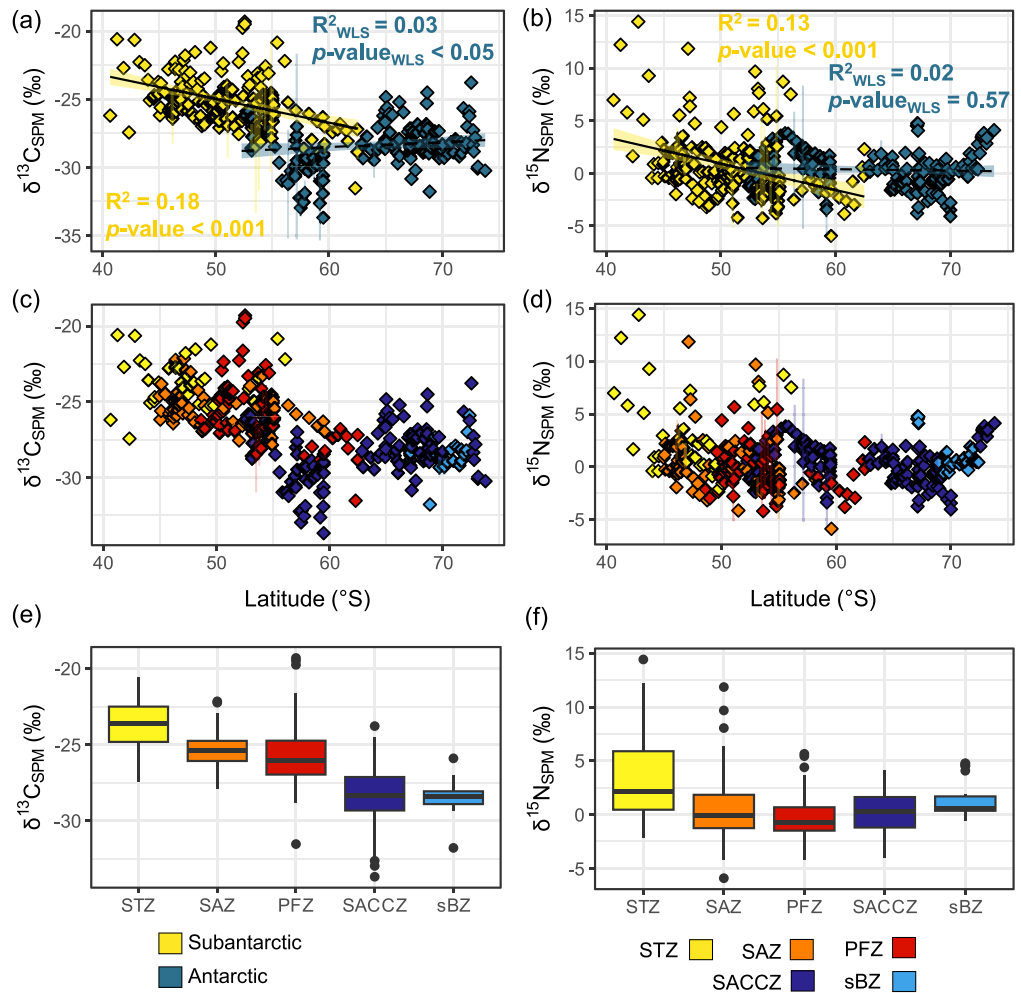
Figure 4. Latitudinal distribution of (a, c, e) $\delta^{13}C_{SPM}$ (‰) and (b, d, f) $\delta^{15}N_{SPM}$ (‰) for surface samples collected during the Antarctic Circumnavigation Expedition. Panels (a)–(b) include linear regression lines (solid) with corresponding confidence intervals (shading) for the Subantarctic data (yellow) and weighted least squares regression lines (dashed) with corresponding confidence intervals (shading) for the Antarctic data (blue). Panels (c)–(f) show the data colored according to hydrographic zone: STZ = Subtropical Zone (yellow), SAZ = Subantarctic Zone (orange), PFZ = Polar Frontal Zone (red), SACCZ = Southern Antarctic Circumpolar Current Zone (dark blue), and sBZ = southern Boundary Zone (light blue). Vertical colored lines indicate ±1SD. Boxplots (panels e and f) show medians (thick horizontal lines), interquartile range (IQR) (50% of the data; box within first and third quartiles), and whiskers (1.5 times the IQR).

For the hydrographic zones in the Subantarctic, significantly higher $\delta^{13}C_{SPM}$ and $\delta^{15}N_{SPM}$ were measured in the STZ ($-23.6^{-22.5}_{-24.8}$‰ and $2.1^{5.9}_{0.5}$‰, respectively) than in the SAZ and PFZ (p-values* <0.001) where the values were similar ($\delta^{13}C_{SPM} = -25.4^{-24.7}_{-26.1}$‰ and $-26.1^{-24.7}_{-27.0}$‰; $\delta^{15}N_{SPM} = -0.1^{+1.8}_{-1.3}$‰ and $-0.8^{+0.7}_{-1.5}$‰; p-values* >0.27; Table 2, Figure 4). The STZ values were also higher than those measured in the SACCZ ($\delta^{13}C_{SPM} = -28.4^{-27.1}_{-29.3}$‰ and $\delta^{15}N_{SPM} = 0.3^{+1.6}_{-1.2}$‰) and for $\delta^{13}C_{SPM}$, higher than in the sBZ ($-28.4^{-28.1}_{-28.8}$‰; p-values* <0.001), while $\delta^{15}N_{SPM}$ in the sBZ was similar ($0.6^{+1.6}_{-1.2}$‰; p-value* = 0.37). For the Antarctic stations, $\delta^{13}C_{SPM}$ and $\delta^{15}N_{SPM}$ in the SACCZ and the sBZ were similar (p-values* >0.05). Additionally, $\delta^{15}N_{SPM}$ in the SACCZ was similar to that measured in the SAZ and PFZ (p-values* >0.18) but different from $\delta^{15}N_{SPM}$ in the STZ (p-values* <0.001).

3.4. Chlorophyll-*a* Concentrations and Phytoplankton Community Composition From Pigment Data

Total Chl-*a* concentrations ranged from 0.01 to 3.7 mg m^{-3} (median of $0.2^{0.4}_{0.1}$ mg m^{-3}) for the entire transect and were significantly higher (p-value* <0.001) in the sBZ and the STZ ($0.4^{1.0}_{0.2}$ mg m^{-3} and $0.3^{0.5}_{0.1}$ mg m^{-3}; p-value* = 0.18) than in the SAZ, PFZ, and SACCZ ($0.2^{0.4}_{0.1}$ mg m^{-3}, $0.2^{0.4}_{0.1}$ mg m^{-3}, and $0.1^{0.3}_{0.1}$ mg m^{-3}; p-values*

Table 3
Median (±IQR) Surface Chlorophyll-a Concentrations (Total Chl-a; mg m⁻³), Relative Contributions to Total Chl-a (%), and Biomass Concentrations (in mg m⁻³ Chl-a; Computed as Relative Contribution × Total Chl-a) of the Various Phytoplankton Size Classes (Pico- (<2 µm), Nano- (2–20 µm), and Micro-phytoplankton (20–200 µm)) Determined From the Pigment Data

Region	Total Chl-a	Micro-phytoplankton (>20 µm)		Nano-phytoplankton (2–20 µm)		Pico-phytoplankton (0–2 µm)	
	mg m⁻³	%	mg m⁻³	%	mg m⁻³	%	mg m⁻³
Subantarctic	0.2 ± 0.3 (208)	43.1 ± 29.8 (215)	0.1 ± 0.1 (208)	56.4 ± 27.0 (215)	0.1 ± 0.1 (208)	0.7 ± 1.8 (215)	0.0 ± 0.0 (208)
Antarctic	0.2 ± 0.3 (169)	72.8 ± 27.4 (169)	0.1 ± 0.2 (169)	26.1 ± 27.4 (169)	0.1 ± 0.1 (169)	0.0 ± 0.4 (169)	0.0 ± 0.0 (169)
STZ	0.3 ± 0.4 (39)	24.5 ± 14.3 (45)	0.1 ± 0.2 (39)	72.3 ± 12.3 (45)	0.2 ± 0.2 (39)	2.7 ± 2.7 (45)	0.0 ± 0.0 (39)
SAZ	0.2 ± 0.3 (81)	35.4 ± 20.3 (82)	0.1 ± 0.1 (81)	62.3 ± 18.4 (82)	0.1 ± 0.1 (81)	0.8 ± 1.7 (82)	0.0 ± 0.0 (81)
PFZ	0.2 ± 0.2 (88)	57.1 ± 19.3 (88)	0.1 ± 0.1 (88)	42.7 ± 19.3 (88)	0.1 ± 0.1 (88)	0.0 ± 0.6 (88)	0.0 ± 0.0 (88)
SACCZ	0.1 ± 0.2 (127)	71.2 ± 28.3 (127)	0.1 ± 0.2 (127)	28.8 ± 28.4 (127)	0.1 ± 0.0 (127)	0.0 ± 0.5 (127)	0.0 ± 0.0 (127)
sBZ	0.4 ± 0.8 (42)	81.1 ± 28.3 (42)	0.3 ± 0.7 (42)	18.9 ± 28.3 (42)	0.1 ± 0.1 (42)	0.0 ± 0.0 (42)	0.0 ± 0.0 (42)

Note. In parentheses are the numbers of observations used to calculate the medians. "Subantarctic" Includes the STZ = Subtropical Zone, SAZ = Subantarctic Zone, and PFZ = Polar Frontal Zone, While 'Antarctic" Includes the SACCZ = Southern Antarctic Circumpolar Current Zone and sBZ = Southern Boundary Zone.

>0.05; Table 3 and Figure 5a). Low Chl-*a* was recorded in the open ocean (0.01–0.3 mg m⁻³) while elevated concentrations (>3 mg m⁻³) occurred near Heard Island, Siple Island, and South America. Elevated Chl-*a* (1–2 mg m⁻³) was also measured at the mouth of the Ross Sea and near the Mertz Glacier.

The contributions (%) of the different phytoplankton size classes to total Chl-*a* derived from the HPLC data varied across the transect, from 11% to 99% for the micro-phytoplankton, <1%–89% for the nano-phytoplankton, and 0%–13% for the pico-phytoplankton (Figures 5b–5d, Figure S7 in Supporting Information S1, Table 3). The contribution of the micro-phytoplankton increased poleward (from $24.5^{33.4}_{19.1}\%$ in the STZ to $81.1^{90.7}_{62.4}\%$ in the sBZ) as the nano-phytoplankton contribution declined (from $72.3^{75.5}_{63.2}\%$ in the STZ to $18.9^{37.6}_{9.3}\%$ in the sBZ; Figure 5b). Pico-phytoplankton contributed $2.7^{4.5}_{1.7}$ and $0.8^{1.8}_{0.1}\%$ of the total Chl-*a* in the STZ and the SAZ, respectively, but in the PFZ, SACCZ, and sBZ, their median contribution was negligible. Consequently, the Subantarctic and Antarctic Oceans were dominated by nano-phytoplankton ($56.4^{68.5}_{41.5}\%$) and micro-phytoplankton ($72.8^{83.1}_{55.7}\%$), respectively. Micro-phytoplankton contributions (>75%) were highest near Heard Island, throughout Leg2, and between the South Sandwich and Bouvet Islands (Figure 5c), while nano-phytoplankton were dominant near South Africa and Tasmania, in the open ocean waters of Leg1, and between South America and South Georgia (Figure 5d).

CHEMTAX analysis revealed that where nano-phytoplankton contributed >55% of the total biomass, haptophytes were dominant ($0.08^{0.15}_{0.04}$ mg m⁻³ of Chl-*a* and $53.5^{61.4}_{48.6}\%$ of total Chl-*a*), followed by nano-sized diatoms ($0.02^{0.04}_{0.00}$ mg m⁻³ and $13.4^{21.6}_{5.3}\%$) (Figures 5e and 5f; Text S6 in Supporting Information S1). In contrast, where micro-phytoplankton contributed >55% of the biomass, diatoms were dominant ($0.15^{0.32}_{0.05}$ mg m⁻³ of Chl-*a* and $60.7^{72.8}_{49.0}\%$ of total Chl-a), followed by haptophytes ($0.05^{0.12}_{0.02}$ mg m⁻³; $28.0^{38.6}_{19.6}\%$) and dinoflagellates ($0.0–0.43$ mg m⁻³; $2.7^{4.8}_{1.7}\%$).

Total micro-phytoplankton abundances ranged from 2 to 12,056 cells L⁻¹ (average of 1,773 ± 2,393 cells L⁻¹ and median of 880^{2022}_{217} cells L⁻¹ for the transect), with 119 species of diatoms, 21 species of dinoflagellates, and 2 species of silicoflagellates identified. Diatom abundances ranged from 0 to 11,972 cells L⁻¹, with diatoms dominating at most stations and accounting for an average of 82.5 ± 30.6% of the micro-phytoplankton (Figure 6a). Maximum diatom abundances occurred between South Sandwich and Bouvet Islands, with high abundances also observed near the PEIs, Kerguelen, and Heard Islands (Figures 6b and 7a). Diatom abundances were particularly low (0–200 cells L⁻¹) in the open ocean over the Indian archipelago, at the end of Leg1, and for most of Leg2. Dinoflagellate abundances ranged from 0 to 762 cells L⁻¹, with dinoflagellates accounting for 17.1 ± 30.7% of the micro-phytoplankton (Figure 6c). Near the end of Leg1 and east of South America, the dinoflagellate contribution increased to 70%–100%, with abundances of >200 cells L⁻¹ (and a maximum abundance near Tasmania of 762 cells L⁻¹), while for much of Leg1 and Leg2, dinoflagellate abundances were ≤20 cells L⁻¹. Silicoflagellates were rare, averaging 4 ± 23% of the total micro-phytoplankton and reaching a maximum abundance near the PEIs of 55.6 cells L⁻¹ (data not shown).
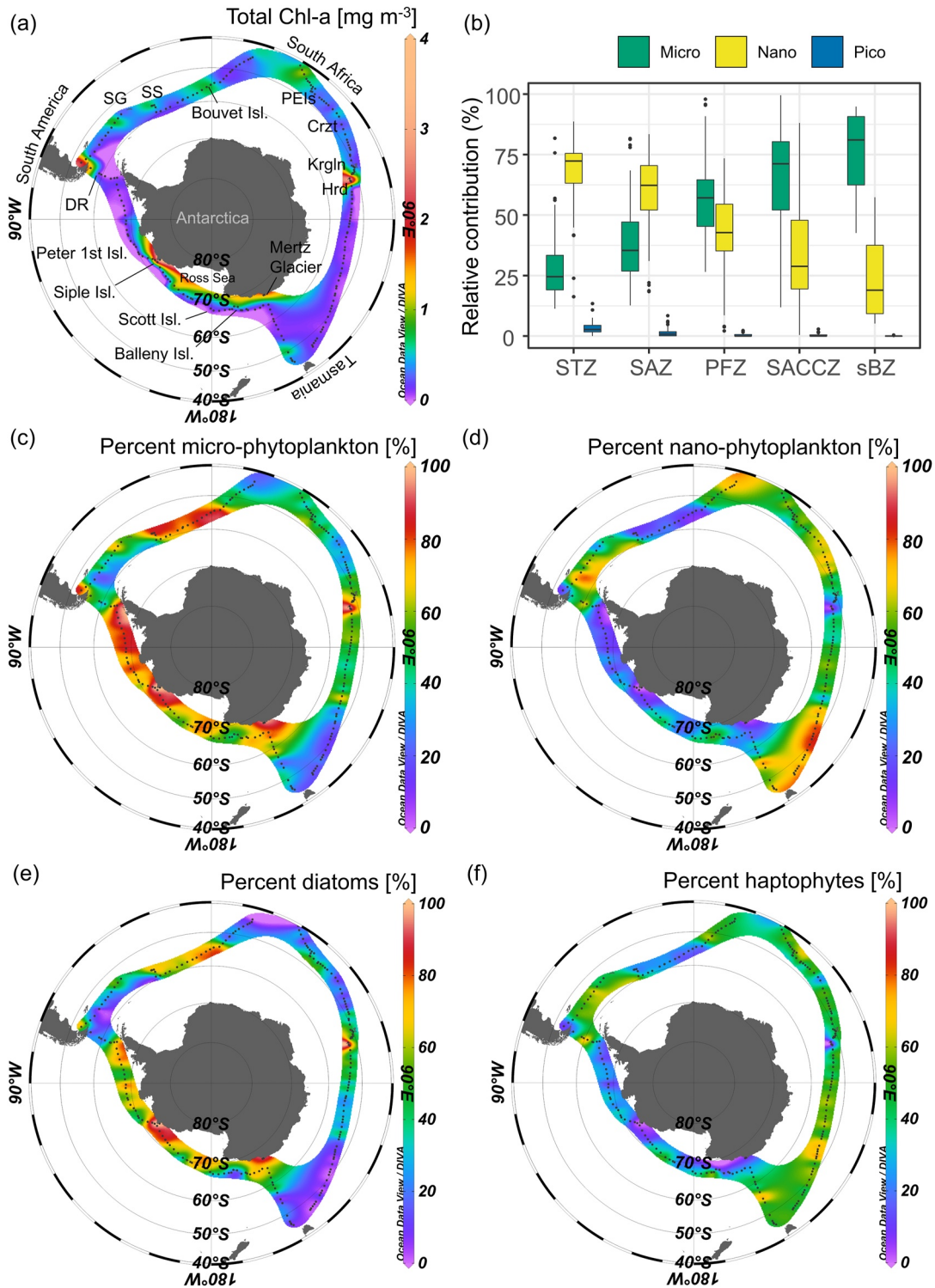
Figure 5. (a) Surface concentrations of total chlorophyll-*a* (Chl-a; mg m^{-3}); (b) boxplots showing the relative contributions (%) of the three phytoplankton size classes to total Chl-*a* in each hydrographic zone (pico- (<2 μm; blue), nano- (2–20 μm; yellow), and micro-phytoplankton (20–200 μm; green)); and the % contribution to total Chl-*a* of (c) micro-phytoplankton, (d) nano-phytoplankton, (e) diatoms, and (d) haptophytes. The islands visited during the cruise are indicated on panel (a): PEIs = Prince Edward Islands, Crzt = Crozet Island, Krgln = Kerguelen Island, Hrd = Heard Island, DR = Diego Ramírez Island, SG = South Georgia, and SS = South Sandwich Islands. Boxplots (panel (b)) show medians (thick horizontal lines), interquartile range (IQR) (50% of the data; box within first and third quartiles), and whiskers (1.5 times the IQR). STZ = Subtropical Zone, SAZ = Subantarctic Zone, PFZ = Polar Frontal Zone, SACCZ = Southern Antarctic Circumpolar Current Zone, and sBZ = southern Boundary Zone. The pigment data used to generate these plots are from Antoine et al. (2020).
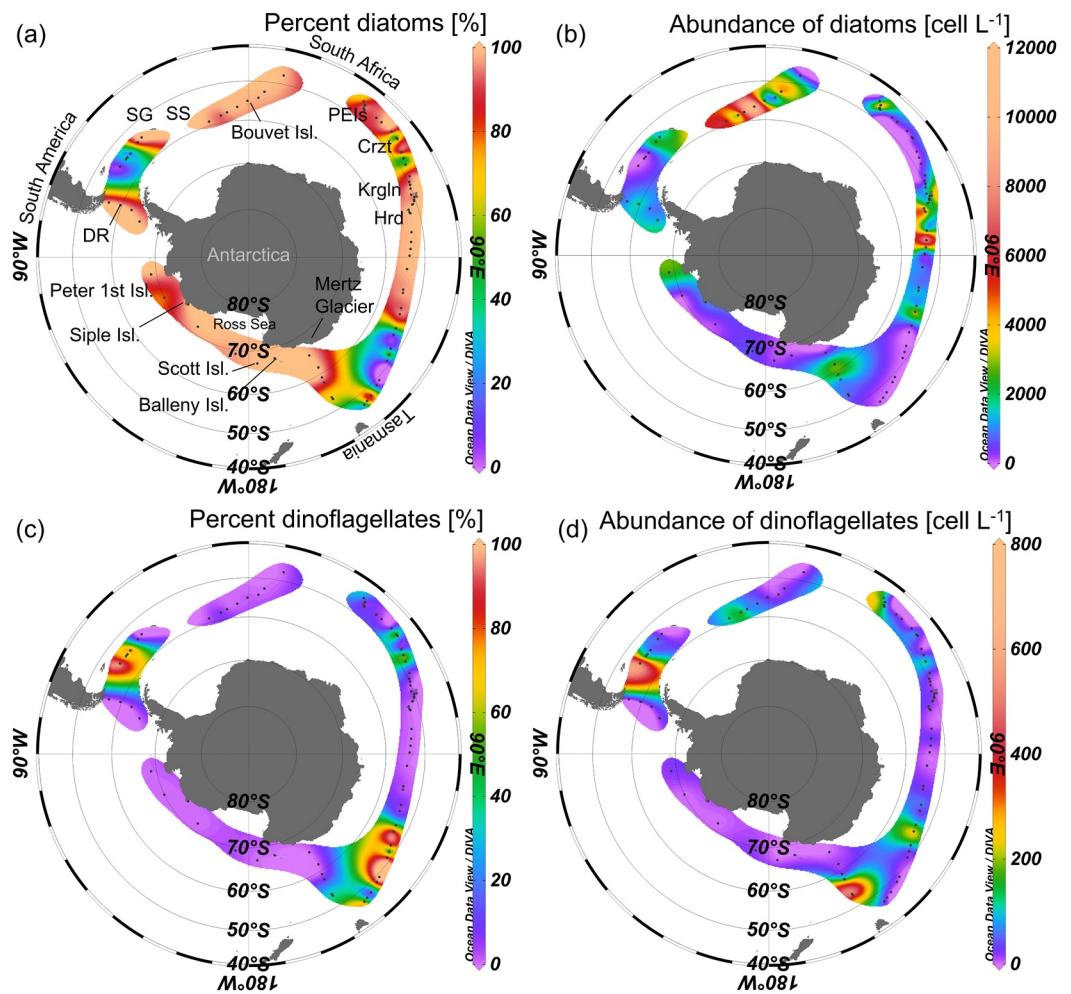
Figure 6. Surface distribution of the percent contribution (a, c; %) to the micro-phytoplankton and total abundances (cells L^{-1}; b, d) of (a)–(b) diatoms and (c)–(d) dinoflagellates. The islands visited during the cruise are indicated on panel (a): PEIs = Prince Edward Islands, Crzt = Crozet Island, Krgln = Kerguelen Island, Hrd = Heard Island, DR = Diego Ramírez Island, SG = South Georgia, and SS = South Sandwich Islands.

In terms of micro-phytoplankton species, *Fragilariopsis kerguelensis* (Figure S9a in Supporting Information S1) dominated the diatom communities (average of 56 ± 28% of total diatoms), reaching particularly high abundances near the PEIs and Kerguelen Island (1,000–5,556 cells L^{-1}; Figures 7a–7c). By contrast, the high diatom abundances near Heard Island (three stations) were due to *Odontella weissflogii* and *Eucampia antarctica* var. *antarctica* (Figure S9c in Supporting Information S1) (1,895 and 1,519 cell L^{-1}, respectively), while the high abundances between the South Sandwich and Bouvet Islands were largely due to *Chaetoceros atlanticus* (3,264 ± 2,212 cells L^{-1}, ~40%) and *F. kerguelensis* (1,861 ± 1,254 cells L^{-1}, ~20%).

Micro-phytoplankton species richness was higher in the SAZ, PFZ, and SACCZ (108, 101, and 72 species, respectively) than in the STZ and sBZ (9 and 8 species), noting that of the 83 stations sampled for micro-phytoplankton, there were 5 in the STZ, 33 in the SAZ, 26 in the PFZ, 18 in the SACCZ, and one in the sBZ (Table S1 in Supporting Information S1). Excluding the sBZ (one station only), the most diverse micro-phytoplankton communities occurred in the PFZ (H' of $1.2_{0.9}^{1.4}$) and SACCZ (H' of $1.0_{0.7}^{1.5}$), followed by the SAZ (H' of $0.9_{0.6}^{1.2}$) and STZ (H' of $0.7_{0.6}^{0.9}$).

3.5. Estimates of f_{new}

For the 269 observations to which we applied our isotope model (Text S2 in Supporting Information S1), f_{new} ranged from −7.0 to 35.2, with 54 values $\notin$ (0, 1). Most of these values occurred in the STZ and near or
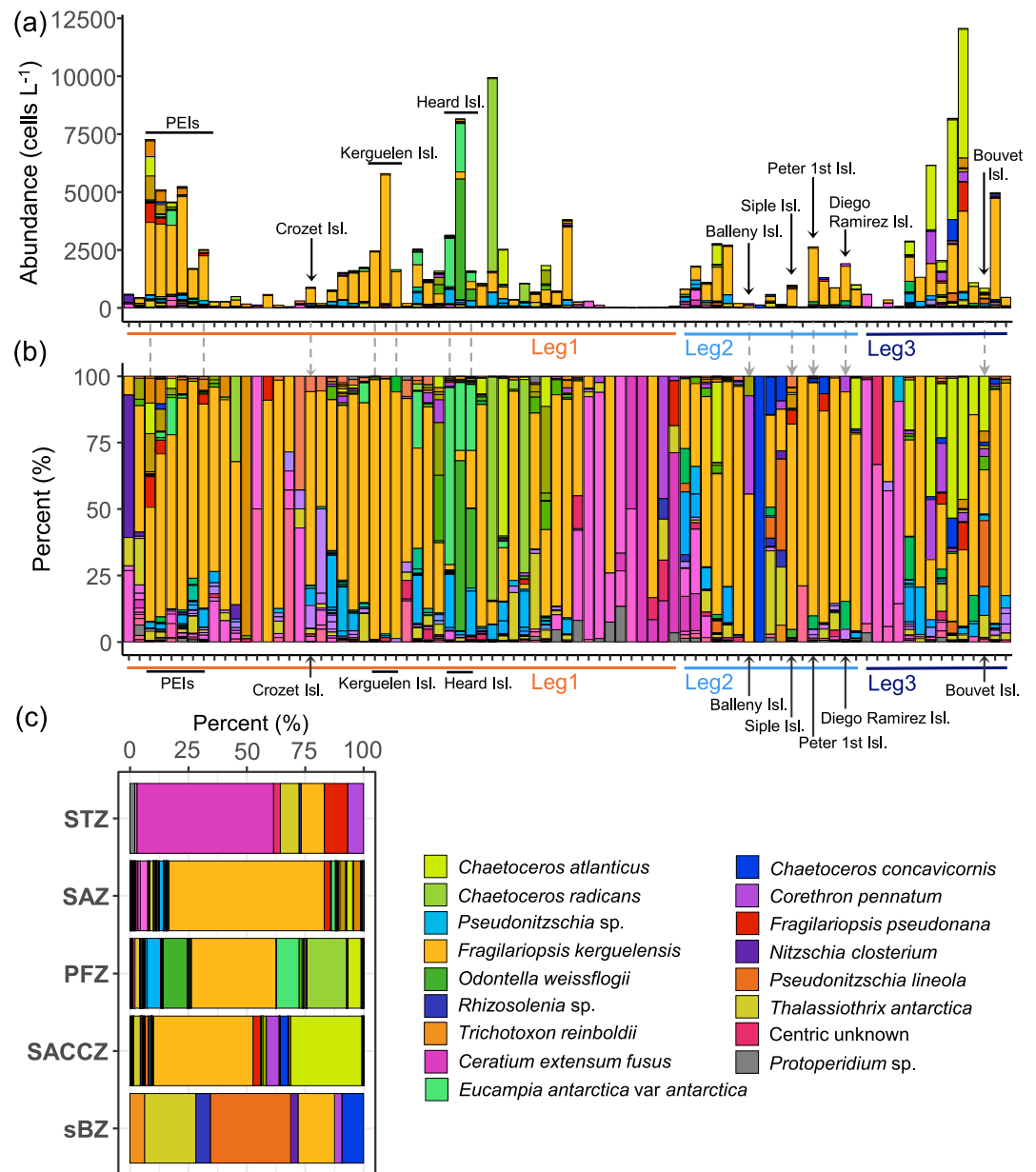
Figure 7. (a) Abundance (cells L^{-1}) and (b)–(c) contribution (%) of different micro-phytoplankton species at each station (b) and in each hydrographic zone (c): STZ = Subtropical Zone, SAZ = Subantarctic Zone, PFZ = Polar Frontal Zone, SACCZ = Southern Antarctic Circumpolar Current Zone, and sBZ = southern Boundary Zone. Vertical arrows indicate islands, with PEIs = Prince Edward Islands, and horizontal lines denote the cruise legs. The percent contribution in panel (c) was estimated from the average abundance of the different micro-phytoplankton species counted in each zone.

downstream of land masses, islands, or regions of sea-ice melt (Figure S14 in Supporting Information S1) where the Rayleigh model requirement of a closed system was violated (e.g., by intermittent upward or lateral mixing of subsurface NO_3^- or allochthonous nutrient inputs). Excluding the out-of-range values yielded 215 estimates of $f_{\text{new}} \in (0, 1)$, ranging from 0.07 to 0.99 ($0.41_{0.31}^{0.60}$; Figure 8, Table 4). f_{new} increased from the STZ ($0.30_{0.24}^{0.43}$) to the SAZ, PFZ, and SACCZ ($0.37_{0.31}^{0.50}$, $0.43_{0.33}^{0.53}$, and $0.41_{0.32}^{0.63}$, respectively; all estimates statistically similar; p-values* >0.1), while in the sBZ, f_{new} was considerably higher ($0.60_{0.46}^{0.66}$) (Figures 8b and Table 4). Values of $f_{\text{new}} > 0.7$ were estimated near the PEIs, at the mouth of the Ross Sea, at Scott and Siple Islands, between the South Sandwich and Bouvet Islands, and downstream of South America, with $f_{\text{new}} > 0.9$ near Kerguelen and Heard and to the east
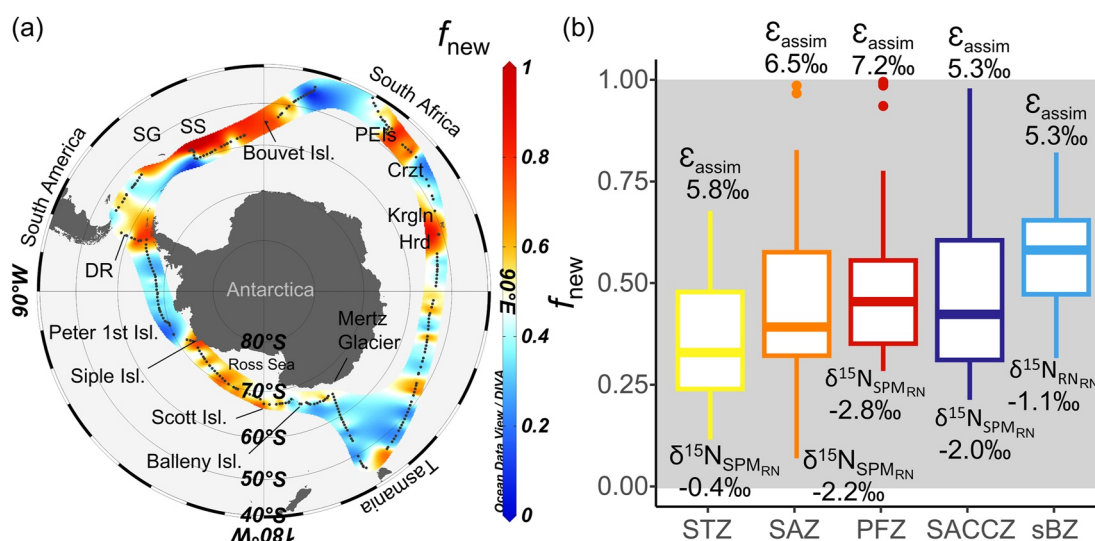
Figure 8. (a) Fraction of phytoplankton growth fueled by new NO_3^- (f_{new}) and (b) boxplots of f_{new} for each hydrographic zone: STZ = Subtropical Zone (yellow), SAZ = Subantarctic Zone (orange), PFZ = Polar Frontal Zone (red), SACCZ = Southern Antarctic Circumpolar Current Zone (dark blue), sBZ = southern Boundary Zone (light blue). The islands visited during the cruise are indicated on panel (a): PEIs = Prince Edward Islands, Crzt = Crozet Island, Krgln = Kerguelen Island, Hrd = Heard Island, DR = Diego Ramírez Island, SG = South Georgia, and SS = South Sandwich Islands. The boxplots (panel (b)) show medians (thick horizontal lines), interquartile range (IQR) (50% of the data; box within first and third quartiles), and whiskers (1.5 times the IQR). Numbers at the top of the boxplots are the median NO_3^- assimilation isotope effects derived for each zone (ε_{assim}; Equation 8) while the numbers at the bottom are the median $\delta^{15}N$ computed for regenerated N ($\delta^{15}N_{SPM_{RN}}$; Equation 3).

of the South Sandwich Islands. In addition, values >0.5 were estimated for the Drake Passage and near the Mertz Glacier, while values <0.5 characterized much of the open ocean, particularly in the STZ.

3.6. Principal Component Analysis

The first and the second principal components (PC1 and PC2) together explained 52.8% of the variance, with the data clustering according to hydrographic zone (Figure 9). Observations in the STZ and SAZ were associated with higher values of SST, $\delta^{13}C_{SPM}$, $\delta^{15}N_{SPM}$, $\delta^{15}N_{SPM_{new}}$, POC:PON, $\delta^{15}N$ of the NO_3^- source (W-S and 200–300 m; $\delta^{15}N_{source}$), and with a higher relative contribution to the Chl-a biomass of nano- and pico-phytoplankton (F-nano and F-pico, respectively). The SACCZ and sBZ stations were negatively associated with these variables. The PCA revealed a generally positive relationship for the SAZ and PFZ with pCO_2 and a slight negative relationship with f_{new}. Data from the SACCZ and sBZ were associated with higher concentrations of SiO_4^{4-}, PO_4^{3-}, NH_4^+, and NO_3^-, and higher relative contributions of micro-phytoplankton (F-micro) to the Chl-a biomass. Observations at the extreme latitudes (a few from the STZ and many from the sBZ) were associated with higher concentrations of POC, PON, and Chl-a, high values of $\delta^{15}N_{SPM}$, $\delta^{15}N_{SPM_{new}}$, fCO_2, and pH, and low pCO_2. Many observations from the sBZ and some from the SACCZ were slightly positively correlated with f_{new}. Data from stations near the islands and continents did not show particular patterns, except for stations at Siple Island, which were positively associated with fCO_2, pH, $\delta^{15}N_{SPM}$, $\delta^{15}N_{SPM_{new}}$, and Chl-a, POC, and PON biomass, with a slight positive relationship with f_{new} and the contribution of micro-phytoplankton to Chl-a (F-micro).

4. Discussion

4.1. Isotopic Differences in SPM Among Southern Ocean Hydrographic Zones Reflect Different Biogeochemical Regimes

4.1.1. Spatial Variability in $\delta^{13}C_{SPM}$

During photosynthesis, phytoplankton preferentially fix ^{12}C-bearing CO_2, producing biomass (SPM) that is lower in $\delta^{13}C$ than the CO_2 substrate (O'Leary, 1981). The remineralization of this SPM returns low-$\delta^{13}C$ CO_2 to the dissolved inorganic carbon (DIC) pool (e.g., McCorkle et al., 1985) such that upwelling of deeper waters lowers the $\delta^{13}C$ of surface DIC (Gruber et al., 1999). The extent to which phytoplankton discriminate against $^{13}CO_2$

Table 4
Inputs to and Outputs of the Rayleigh and Isotope Mixing Models

Region	ε_{assim} (‰)	MLD_{summer} (m)	MLD_{winter} (m)	$NO_3^-{}_{(W-S)}$ (μM)	$\delta^{15}N\ NO_3^-{}_{(W-S)}$ (‰)	$NO_3^-{}_{(200-300)}$ (μM)	$\delta^{15}N\ NO_3^-{}_{(200-300)}$ (‰)	$\delta^{15}N_{SPM_{MRN}}$ (‰)	n	$\delta^{15}N_{SPM_{new}}$ (‰)	f_{new}
Subantarctic	6.5 ± 2.0 (189)	35.2 ± 28.8 (189)	105.0 ± 30.0 (189)	23.3 ± 6.2 (189)	6.7 ± 1.1 (189)	26.0 ± 9.5 (196)	5.7 ± 1.0 (187)	−1.6 ± 3.1 (194)	101	1.1 ± 2.4	0.38 ± 0.20
Antarctic	5.3 ± 0.5 (158)	18.6 ± 7.7 (158)	55.0 ± 20.0 (158)	28.8 ± 1.9 (158)	6.1 ± 0.5 (158)	34.0 ± 1.0 (158)	4.9 ± 0.1 (158)	−1.1 ± 2.6 (166)	114	1.8 ± 0.8	0.43 ± 0.32
STZ	5.8 ± 1.1 (34)	26.2 ± 16.3 (34)	105.0 ± 40.0 (34)	14.2 ± 4.9 (34)	8.2 ± 0.6 (34)	15.4 ± 4.7 (38)	6.8 ± 0.5 (37)	0.6 ± 5.4 (37)	23	4.5 ± 3.2	0.30 ± 0.19
SAZ	6.5 ± 1.3 (77)	35.2 ± 18.8 (77)	105.0 ± 20.0 (77)	21.7 ± 3.5 (77)	7.1 ± 0.7 (77)	25.1 ± 5.4 (77)	5.8 ± 0.3 (76)	−1.6 ± 3.1 (76)	39	1.1 ± 1.0	0.37 ± 0.19
PFZ	7.2 ± 2.0 (78)	45.0 ± 28.8 (78)	105.0 ± 61.5 (78)	26.1 ± 2.7 (78)	6.4 ± 0.5 (78)	31.3 ± 6.5 (81)	5.2 ± 0.2 (78)	−2.3 ± 2.2 (81)	39	0.3 ± 1.1	0.43 ± 0.20
SACCZ	5.3 ± 0.5 (138)	18.6 ± 7.7 (138)	55.0 ± 20.0 (138)	28.7 ± 2.0 (138)	6.2 ± 0.4 (138)	34.0 ± 1.2 (138)	4.9 ± 0.1 (138)	−1.2 ± 2.8 (141)	98	1.8 ± 0.8	0.41 ± 0.32
sBZ	5.3 ± 0.0 (20)	18.6 ± 0.0 (20)	50.0 ± 39.8 (20)	29.0 ± 0.7 (20)	5.9 ± 0.7 (20)	34.3 ± 0.2 (20)	4.9 ± 0.2 (20)	−0.9 ± 1.3 (25)	16	1.6 ± 1.1	0.60 ± 0.21

Note. Medians (±IQR) of the isotope effect of NO_3^- assimilation (ε_{assim}; ‰), summer and winter mixed layer depth (MLD_{summer} and MLD_{winter}; m; from b-SOSE: Mazloff et al., 2010; Verdy & Mazloff, 2017), and the concentration (μM) and $\delta^{15}N$ (‰) of the NO_3^- source (from b-SOSE and Rafter et al. (2019), respectively), taken to be either the water mass between the MLD_{summer} and the MLD_{winter} ($NO_3^-{}_{(W-S)}$ and $\delta^{15}N_{NO_3^-{}_{(W-S)}}$; ‰) or the water mass at 200–300 m ($NO_3^-{}_{(200-300)}$ and $\delta^{15}N_{NO_3^-{}_{(200-300)}}$; ‰) and new N (i.e., NO_3^-) consumed by phytoplankton ($\delta^{15}N_{SPM_{new}}$; ‰), and the fraction of phytoplankton growth fueled by new N (f_{new}). In parentheses and in the column headed n are the number of values used to calculate the medians. Medians of input parameters were calculated from the whole dataset (364 observations) while the medians of the outputs were calculated for the subset of the dataset that met certain criteria (246 observations; Sections S2 and S7 in Supporting Information S1). Values are shown for the Subantarctic and Antarctic Oceans, as well as for the STZ = Subtropical Zone, SAZ = Subantarctic Zone, PFZ = Polar Frontal Zone, SACCZ = Southern Antarctic Circumpolar Current Zone, and sBZ = southern Boundary Zone.

is strongly driven by their growth rate and the ambient pCO_2 (François et al., 1993; Goericke, 1994; Laws et al., 1995). For the same initial pCO_2, a higher growth rate yields less isotopic fractionation and thus a higher $\delta^{13}C_{SPM}$, while for phytoplankton growing at the same rate, higher surface-water pCO_2 is associated with higher fractionation and a lower $\delta^{13}C_{SPM}$ (Gruber et al., 1999; Rau et al., 1991). The $\delta^{13}C$ of the DIC available to phytoplankton will also affect $\delta^{13}C_{SPM}$ as it sets the isotopic baseline for the system (e.g., Tamelander et al., 2009).

We observed a general northward increase in $\delta^{13}C_{SPM}$, of ~12‰ between the Antarctic and the STZ, with a higher median (±IQR) $\delta^{13}C_{SPM}$ in the Subantarctic than the Antarctic (−25.2 ± 2.1‰ vs. −28.4 ± 2.0‰; Figures 4a, 4c and 4e; Figure S15a in Supporting Information S1). This meridional trend has been reported previously and attributed to a northward decrease in isotope fractionation during photosynthesis driven by a decline in surface pCO_2 and higher phytoplankton growth rates (Arteaga et al., 2018; Espinasse et al., 2019; François et al., 1993; Popp et al., 1999). Across the Subantarctic, $\delta^{13}C_{SPM}$ was negatively correlated with pCO_2 ($\rho = -0.40$; Figures 10a and 10b) and (relatedly) positively correlated with pH, fCO_2, and SST ($\rho = 0.50, 0.53, 0.37$; p-values <0.05; Figure S17 in Supporting Information S1), which confirms that pCO_2 was a dominant driver of Subantarctic $\delta^{13}C_{SPM}$. However, we also observed strong deviations from the expected pCO_2-driven latitudinal trend in $\delta^{13}C_{SPM}$. For instance, $\delta^{13}C_{SPM}$ reached a minimum in the southern PFZ and northern SACCZ (55–60°S; median of −29.3 ± 3.2‰, reaching −33.7‰). Furthermore, incidences of anomalously high $\delta^{13}C_{SPM}$ relative to expectations from pCO_2 were apparent near and/or downstream of some of the islands (e.g., the PEIs) and off South America, while in the SACCZ and sBZ where pCO_2 was the lowest, we observed anomalously low values of $\delta^{13}C_{SPM}$ (Figures 2f and 3d).

The $\delta^{13}C_{SPM}$ minimum in the PFZ/SACCZ may be related to upwelling of Upper Circumpolar Deep Water (UCDW) south of the ACC (Talley, 2011). UCDW hosts a remineralization-driven high DIC concentration and low DIC-$\delta^{13}C$ (0.2–0.3‰; Kroopnick, 1985; Williams et al., 2021), while the DIC-$\delta^{13}C$ in the upper ~50 m of the Southern Ocean ranges from 0.75 to 1.75‰ in the Antarctic (>55°S) and 1.50–2.25‰ in the Subantarctic (40–55°S) (François et al., 1993; Gruber et al., 1999). Thus, the photosynthesis of relatively low-$\delta^{13}C$ DIC in upwelled UCDW may explain the lower $\delta^{13}C_{SPM}$ in the PFZ/SACCZ region.

Although the range in pCO_2 in the Subantarctic and Antarctic was similar (except for a few incidences of particularly low pCO_2 (23–32 Pa) in the Antarctic; see below), $\delta^{13}C_{SPM}$ differed by ~3‰ between the two regions (Figure 10 and Table 2). Since the median POC:PON ratio of SPM in the Subantarctic (7.4$_{6.8}^{7.9}$) and Antarctic (6.9$_{6.5}^{7.4}$; Figures 3c and Table 2) resembled that expected for actively growing phytoplankton (Garcia et al., 2018), variations in $\delta^{13}C_{SPM}$ can be assumed to predominantly reflect changes in phytoplankton $\delta^{13}C$. The contribution of nano-phytoplankton (particularly haptophytes, likely mainly coccolithophores; Text S6 in Supporting Information S1) to the SPM increased northwards, as did the abundance of large dinoflagellates, while the contribution of the micro-phytoplankton (particularly diatoms) declined (Figures 5–7). These geographical differences in plankton community composition likely influenced the latitudinal trend in $\delta^{13}C_{SPM}$ (Falkowski, 1991; Goericke, 1994; Tuerena et al., 2019).
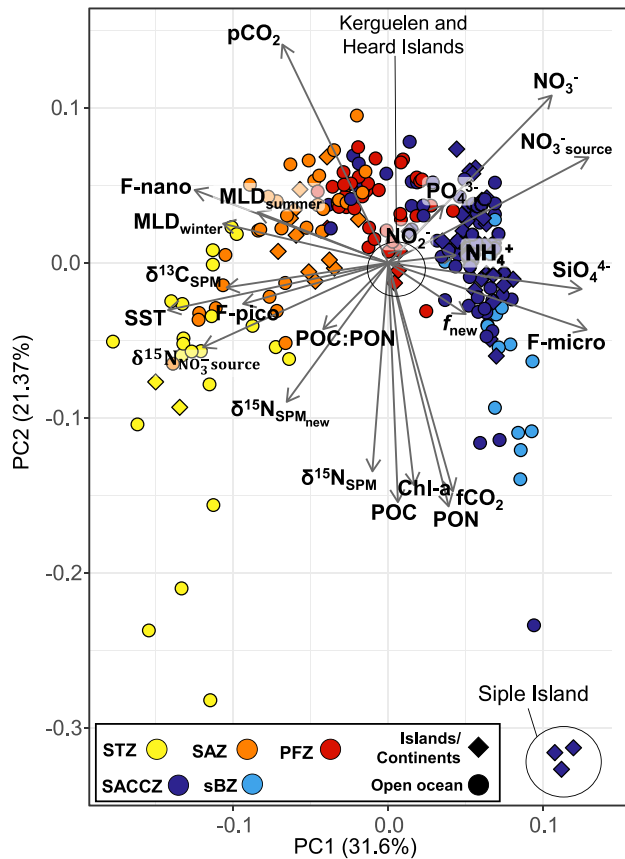
Figure 9. Principal Component Analysis of our dataset (246 observations). Surface parameters considered include observations of sea surface temperature, the concentrations of nitrate (NO_3^-), nitrite (NO_2^-), phosphate (PO_4^{3-}), silicic acid (SiO_4^{4-}), and ammonium (NH_4^+), the partial pressure and air-sea flux of CO_2 (pCO_2 and fCO_2), the concentrations of particulate organic carbon and nitrogen (POC and PON), their molar ratio (POC:PON) and isotopes ($\delta^{13}C_{SPM}$ and $\delta^{15}N_{SPM}$), total chlorophyll-a (Chl-a), and the contributions of micro-, nano-, and pico-phytoplankton to Chl-a (F-micro, F-nano, F-pico) determined from the High Performance Liquid Chromatography data. Modeled parameters are also included: the winter and summer mixed layer depths (MLD_{winter} and MLD_{summer}), the concentration and $\delta^{15}N$ of the NO_3^- source ($NO_3^-_{source}$ and $\delta^{15}N_{NO_3^-source}$), the theoretical $\delta^{15}N$ of phytoplankton biomass produced from the assimilation of NO_3^- ($\delta^{15}N_{SPM_{new}}$), and the fraction of phytoplankton growth fueled by NO_3^- (f_{new}). The symbol colors indicate the hydrographic zones: STZ = Subtropical Zone (yellow), SAZ = Subantarctic Zone (orange), PFZ = Polar Frontal Zone (red), SACCZ = Southern Antarctic Circumpolar Current Zone (dark blue), and sBZ = southern Boundary Zone (light blue), while the symbol shapes indicate stations from the open ocean (circles) versus near the islands and continents (diamonds).

At high pCO_2, diffusion of CO_2 across the cell membrane is rate-limiting to photosynthesis and thus controls isotope fractionation, yielding a low $\delta^{13}C_{SPM}$ (François et al., 1993; Rau et al., 1989). In contrast, at lower pCO_2, fractionation associated with the intra-cellular carbon concentrating mechanism becomes rate-limiting, yielding a higher $\delta^{13}C_{SPM}$ (François et al., 1993; Raven et al., 2008). While all phytoplankton contain the RuBisCO enzyme, which has a large isotope effect (of ~29‰; Raven & Johnston, 1991; Roeske & O'Leary, 1984), some species also have a β-carboxylation enzyme, such as PEPcarboxylase (PEPc), which is typically found in coccolithophores (Tsuji et al., 2009), dinoflagellates, and other small (pico- and nano-) phytoplankton, or PEPcarboxykinase (PEPk), which is found in diatoms (Descolas-Gros & Fontugne, 1985; Descolas-Gros & Oriol, 1992). PEPc catalyzes the fixation of bicarbonate (HCO_3^-), which has a higher $\delta^{13}C$ (~1.5‰) than CO_2 (~−10‰), the latter fixed by PEPk (François et al., 1993; Mook et al., 1974). In addition, PEPc has a smaller intrinsic isotope effect than PEPk (~2‰ vs. >20‰; Arnelle & O'Leary, 1992; Guy et al., 1989; O'Leary, 1981). As such, while the northward decrease in pCO_2 may explain much of the latitudinal rise in $\delta^{13}C_{SPM}$, the coincident increase in haptophytes and large dinoflagellates may have also raised $\delta^{13}C_{SPM}$ because of the lower net fractionation associated with PEPc carboxylation.

The higher $\delta^{13}C_{SPM}$ near the Subantarctic islands and continents could be due to the coincidence of low pCO_2 and the composition and growth rates of the in situ phytoplankton. During fast-growing blooms, large diatoms have been observed to have a higher $\delta^{13}C_{SPM}$ than smaller cells (Fry & Wainright, 1991), with Nakatsuka et al. (1992) reporting a positive correlation between phytoplankton growth rate and $\delta^{13}C_{SPM}$. However, Berg et al. (2011) observed a low $\delta^{13}C_{SPM}$ for diatoms growing rapidly following iron fertilization in the open PFZ, with $\delta^{13}C_{SPM}$ increasing later as the post-bloom phytoplankton community became more diverse. In our study, phytoplankton biomass at Heard Island was over six-times higher than over the Atlantic archipelago and the rest of the Indian archipelago (Figure 5a). High phytoplankton growth rates at Heard Island, stimulated by an island mass effect-related input of nutrients (e.g., Jena, 2016) (Figures 2a–2e), may have reduced net isotope fractionation, yielding substantially higher values of $\delta^{13}C_{SPM}$ (− 19.7$_{−20.7}^{−19.6}$‰) than at the Atlantic archipelago (− 29.1$_{−29.8}^{−28.5}$‰) and over the rest of the Indian archipelago (− 25.0$_{−25.9}^{−24.4}$‰).

The $\delta^{13}C_{SPM}$ differences among the islands were unlikely due only to pCO_2 and growth rate, however. The $\delta^{13}C_{SPM}$ at the Indian archipelago (excluding Heard Island) was higher than at the Atlantic archipelago, despite both regions having similar pCO_2 and phytoplankton biomass. Micro-phytoplankton (presumably mainly diatoms) were the main contributors to total Chl-a at the Atlantic archipelago (73 ± 10%; Figure 5) while at the Indian archipelago, the micro-phytoplankton contribution was lower, 49 ± 15% and 31 ± 6% at the PEIs and Crozet (increasing to 94 ± 3% at Heard Island). Two distinct diatom communities were present at the Indian archipelago, one dominated by *F. kerguelensis* (most of the archipelago) and the second dominated by *O. weissflogii* and *E. antarctica* var. *antarctica* (Heard Island).

Assuming that iron was not limiting near the islands (e.g., Schallenberg et al., 2018), the distinct phytoplankton communities of the Atlantic and Indian archipelagos (excluding Heard Island) may be analogous to the two assemblages described by Berg et al. (2011). In that study, rapidly growing *Chaetoceros* spp. dominated the assemblage shortly after iron addition, with a $\delta^{13}C_{SPM}$ that was slightly higher than prior to fertilization. The phytoplankton community then evolved into a more diverse assemblage of smaller cells including haptophytes. This change coincided with a further ~1.5‰ rise in $\delta^{13}C_{SPM}$, attributed to a higher ratio of PEPc to RuBisCO

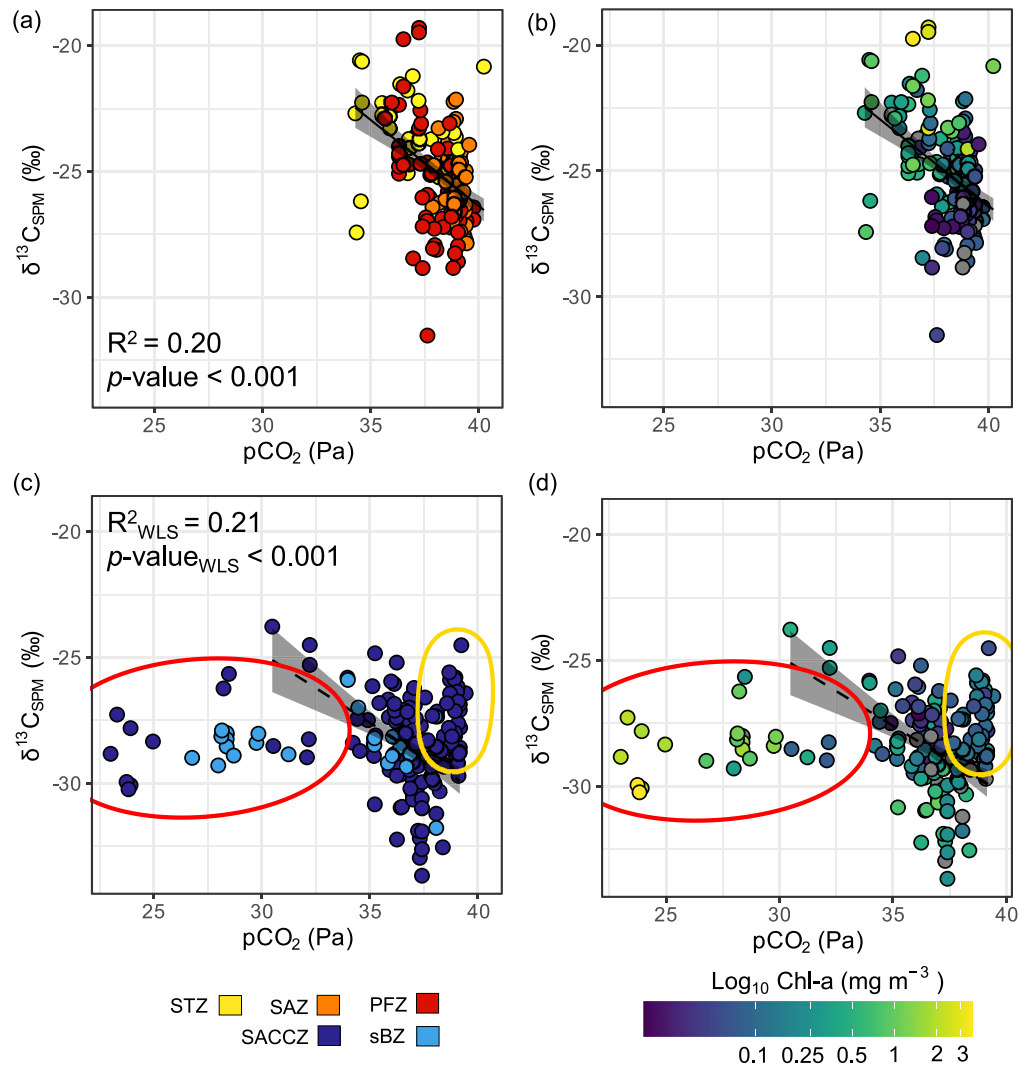**Figure 10.** Relationship between the surface partial pressure of CO_2 (pCO_2; Pa) and $\delta^{13}C_{SPM}$ (‰) in the (a–b) Subantarctic and (c–d) Antarctic Oceans. Symbol colors in the left-hand panels (a, c) show the hydrographic zones: STZ = Subtropical Zone (yellow), SAZ = Subantarctic Zone (orange), PFZ = Polar Frontal Zone (red), SACCZ = Southern Antarctic Circumpolar Current Zone (dark blue), sBZ = southern Boundary Zone (light blue), while symbol colors in the right-hand panels (b, d) show total chlorophyll-*a* concentrations (High Performance Liquid Chromatography data) on a $\log_{10}$ scale (Log_{10} Chl-a; mg m^{-3}). In panels (c) and (d), the ellipses highlight notable deviations from the expected pCO_2-$\delta^{13}C_{SPM}$ relationship. Solid and dashed lines show the ordinary least squares regression and weighted least squares (WLS) regression lines, respectively, with the shading showing the 95% confidence intervals. The WLS models were fitted using the inverse of the variance of the residuals as weights.

activity and thus a decline in net isotopic fractionation. Our data may be similarly explained—we measured a higher $\delta^{13}C_{SPM}$ in waters dominated by a smaller, more diverse phytoplankton community (the Indian archipelago excluding Heard Island) and a lower $\delta^{13}C_{SPM}$ coincident with the dominance of large diatoms including *Chaetoceros* spp. (Atlantic archipelago).

From the APF to Antarctica, $\delta^{13}C_{SPM}$ was near-constant ($-28.4^{-27.3}_{-29.3}$‰; Figures 4a, 4c, and 4e) and not correlated with pCO_2 when all measurements from the SACCZ and sBZ were considered ($\rho = -0.02$, *p*-value = 0.52; Figure S18 in Supporting Information S1). However, a closer inspection of the data reveals three different relationships of $\delta^{13}C_{SPM}$ to pCO_2 (Figures 10c and 10d). In the SACCZ and sBZ, $\delta^{13}C_{SPM}$ was significantly negatively correlated with pCO_2 between 32 and 38 Pa ($\rho = -0.40$, *p*-value <0.001), as was observed for the Subantarctic. Additionally, at the highest pCO_2 (~39–40 Pa; data from the SACCZ only), $\delta^{13}C_{SPM}$ was anomalously high (>-28‰;

yellow ellipse in Figures 10c and 10d) while at a pCO$_2$ of 23–32 Pa, δ^{13}C$_{SPM}$ was anomalously low (−30‰ to −28‰; red ellipse in Figures 10c and 10d) relative to the expected relationship of δ^{13}C$_{SPM}$ to pCO$_2$.

As outlined above, Berg et al. (2011) reported a lower δ^{13}C$_{SPM}$ for large, iron-replete diatoms than for the more mixed and smaller phytoplankton cells that succeeded them. This dynamic may explain the anomalously low δ^{13}C$_{SPM}$ at low pCO$_2$ observed near the Mertz Glacier, Ross Sea mouth, and Siple and Peter 1st Islands (red ellipse in Figures 10c and 10d). Here, biomass was high (Figures 3a–3b, 5$^{3a–3b}$, and 10d) and the phytoplankton community comprised near-exclusively large diatoms (mostly *F. kerguelensis*; Figure 7). However, the rapid growth rates typically associated with high biomass production occur with relatively low isotopic fractionation (Laws et al., 1995), yielding higher values of δ^{13}C$_{SPM}$, as at Heard Island (Figures 5 and 6). The δ^{13}C$_{SPM}$ difference between Heard Island and the Mertz Glacier/Ross Sea/Siple/Peter 1st Island region may thus involve the rate of CO$_2$ resupply to surface waters rather than being predominantly due to growth rate. At Heard Island, CO$_2$ depletion by phytoplankton may have been faster than its rate of resupply, causing δ^{13}C$_{SPM}$ to increase due to ^{13}C-enrichment of the in situ CO$_2$ (Deuser, 1970; Villinski et al., 2008). Such ^{13}C-enrichment is typically negligible because rapid equilibration of CO$_2$ and HCO$_3^-$ essentially renders the entire (large) DIC pool available to phytoplankton (Tortell et al., 1997, 2008). However, if phytoplankton growth is particularly rapid, as is possible near Heard Island where conditions are extremely favorable (Mongin et al., 2008, 2009), CO$_2$ can be so quickly depleted as to raise its δ^{13}C (Deuser, 1970). In contrast, the Mertz Glacier/Ross Sea/Siple/Peter 1st Island region was characterized by the highest fCO$_2$ of the Antarctic Ocean (>10 mg m^{-2} h^{-1} from atmosphere to ocean; Figure S5 in Supporting Information S1), likely induced by high biological activity (Tagliabue & Arrigo, 2016) and intense CO$_2$ dissolution driven by low SSTs and enhanced ice melt (Fransson et al., 2011; Tortell et al., 2012). The resultant high rate of CO$_2$ resupply would negate any ^{13}C-enrichment of the in situ CO$_2$ and thus, the SPM (Freeman & Hayes, 1992; Rau et al., 1989).

The anomalously high-pCO$_2$ and high-δ^{13}C$_{SPM}$ (yellow ellipse in Figures 10c and 10d) occurred far downstream of Bouvet and Heard Islands in waters that were influenced by the APF. Phytoplankton biomass was low and comprised ~50% nano-phytoplankton (mostly haptophytes; Figure 5). We suggest that these phytoplankton were mainly a post-bloom, iron-limited community expressing a higher ratio of PEPc to RuBisCO activity, which would have caused lower net isotope fractionation and thus a higher δ^{13}C$_{SPM}$ (Descolas-Gros & Fontugne, 1985, 1990).

To statistically validate the influence of phytoplankton community composition, alongside that of pCO$_2$, on the spatial distribution of δ^{13}C$_{SPM}$, we conducted a Generalized Additive Model analysis (see Text S7 in Supporting Information S1). The results confirm that community composition strongly influences surface δ^{13}C$_{SPM}$ across the Southern Ocean, with elevated fractions of nano-phytoplankton clearly associated with a higher δ^{13}C$_{SPM}$ and higher proportions of micro-phytoplankton corresponding to a lower δ^{13}C$_{SPM}$.

4.1.2. Spatial Variability in δ^{15}N$_{SPM}$

In our dataset, δ^{15}N$_{SPM}$ decreased by ~3‰ from the STZ (2.1 ± 5.4‰ [median ± IQR]) to the SAZ and PFZ where it reached a minimum (−0.1 ± 3.1‰ and −0.8 ± 2.2‰, respectively), before increasing again into the Antarctic (SACCZ = 0.3 ± 2.8‰ and sBZ = 0.6 ± 1.3‰; Table 2; Figures 3e, 4b, 4d, and 4f). For the entire transect, δ^{15}N$_{SPM}$ was positively correlated with POC, PON, and Chl-*a* (ρ = 0.48, 0.44, and 0.45; *p*-value <0.001), consistent with the expectation that higher biomass accompanies higher rates of productivity and greater NO$_3^-$ utilization, the latter yielding higher values of δ^{15}N$_{SPM}$ (Altabet & Francois, 1994). Generally, the latitudinal trends in δ^{15}N$_{SPM}$ agree well with previous observations (e.g., Espinasse et al., 2019; St John Glew et al., 2021). Using a Bayesian hierarchical spatial model applied to data collected over 50 years, St John Glew et al. (2021) determined that SST and MLD were good predictors of δ^{15}N$_{SPM}$ in the Southern Ocean; however, we observe a positive relationship between δ^{15}N$_{SPM}$ and SST only in the Subantarctic (ρ = 0.37, *p*-value < 0.001; Figure S17 in Supporting Information S1) and a positive correlation with MLD only in the Antarctic (ρ = 0.37, *p*-value < 0.001; Figure S18 in Supporting Information S1). The inconsistency of our findings with those of St John Glew et al. (2021) highlights our lack of mechanistic understanding of the synergistic drivers of δ^{15}N$_{SPM}$ across the Southern Ocean.

The δ^{15}N of phytoplankton biomass depends on the δ^{15}N of the N sources consumed, the extent of consumption of those N sources, and the isotope effect(s) expressed during consumption (Altabet & Francois, 2001; Fawcett et al., 2011; Granger et al., 2004; Sigman et al., 1999). The δ^{15}N of subsurface NO$_3^-$ (i.e., $\delta^{15}N_{NO_3^- \text{ (source)}}$) is influenced by exchange with underlying deep-water NO$_3^-$ and by N-cycle processes occurring in the surface and subsurface during water mass circulation (Rafter et al., 2013; Sigman et al., 2000). South of the SACCF,

lower circumpolar deep water with a $\delta^{15}N$ of 4.8‰ is the ultimate source of NO_3^- to the mixed layer, while north of the SACCF, UCDW supplies NO_3^- with a $\delta^{15}N$ of ~5‰ (Fripiat et al., 2019; Rafter et al., 2013; Sigman et al., 2000; Smart et al., 2015). Partial consumption of NO_3^- in the northward-flowing Antarctic Surface Water that derives from UCDW raises its $\delta^{15}N$, such that the Antarctic Intermediate Water and SAMW that form in the PFZ and SAZ are higher in $\delta^{15}N_{NO_3^-}$ than UCDW (5.7‰ and >6.3‰, respectively; Rafter et al., 2013; Sigman et al., 1999). As these water masses subduct and flow northwards, they become the sub-mixed layer NO_3^- source across much of the Subantarctic. At the same time, surface processes continue to modify subsurface NO_3^- as sinking particles recording the $\delta^{15}N$ of mixed-layer N cycling are remineralized below the mixed layer (Rafter et al., 2013; Sigman et al., 1999).

In our dataset, the $\delta^{15}N_{NO_3^-(source)}$ decreased by ~2‰ from the lower latitudes to the APF (STZ = 8.2 ± 0.7‰, SAZ = 6.8 ± 1.1‰, PFZ = 6.3 ± 0.6‰), after which it remained stable (Antarctic Ocean = 6.1 ± 0.5‰) (Table 4 and Figure S19a in Supporting Information S1). As expected, the $\delta^{15}N_{SPM}$ was generally lower than the $\delta^{15}N_{NO_3^-(source)}$ because of isotope fractionation during NO_3^- assimilation (Sigman et al., 1999), with a median difference (i.e., $\delta^{15}N_{SPM}-\delta^{15}N_{NO_3^-(source)}$) of $-6.3_{-7.7}^{-4.9}$‰ and the highest variability at the lower latitudes (*p*-value <0.05; Figure S19b-c in Supporting Information S1). The large-scale consistency of $\delta^{15}N_{SPM}-\delta^{15}N_{NO_3^-(source)}$ across the Southern Ocean suggests that the $\delta^{15}N$ of NO_3^- is a principal factor controlling $\delta^{15}N_{SPM}$ (Figure S2 in Supporting Information S1).

The $\delta^{15}N_{SPM}$ is also strongly influenced by the $\delta^{15}N$ of regenerated N and the extent to which NO_3^- versus regenerated N are consumed (Fawcett et al., 2011, 2014; Lourey et al., 2003). More negative values of $\delta^{15}N_{SPM}-\delta^{15}N_{NO_3^-(source)}$ are associated with a higher degree of regenerated N consumption (i.e., $f_{new} < 0.5$) and less negative values with proportionally higher NO_3^- consumption (i.e., $f_{new} > 0.5$; Figure S19b-c in Supporting Information S1). This trend is explained by the $\delta^{15}N$ of regenerated N, which is considerably lower than that of the source NO_3^- (i.e., −5–0‰ vs. 5‰–7‰; Checkley & Miller, 1989; Fawcett et al., 2011; Lourey et al., 2003; Sigman et al., 1999).

Our estimates of f_{new} indicate that the degree of NO_3^- consumption increased poleward (Figure 8b). Such a trend could be related to latitudinal changes in nutrient concentrations, light and MLD, and/or phytoplankton community composition. Indeed, f_{new} was (weakly) positively correlated with the relative contributions of micro-phytoplankton to Chl-a, likely due to the dominance of the micro-phytoplankton by diatoms (Figure 5), which are NO_3^- specialists. Indeed, diatoms have been shown to take up NO_3^- faster than other phytoplankton groups at comparable substrate concentrations (Eppley et al., 1969; Hildebrand & Dahlin, 2000; Paasche et al., 1984), often achieving higher NO_3^- uptake and reduction rates than required for growth, especially in cold, NO_3^--rich environments (Lomas & Glibert, 1999, 2000). f_{new} was negatively correlated with the contribution to Chl-*a* of nano-phytoplankton, which typically show a higher affinity for NH_4^+ than micro-phytoplankton (Probyn, 1985; Stirnimann et al., 2021; Wafar et al., 2004). The apparent preference of nano-phytoplankton for NH_4^+ over NO_3^- can be explained by their higher surface-area-to-volume ratio, which makes them more competitive for scarce nutrients than the larger diatoms (Marañón, 2015).

Of our 269 measurements of $\delta^{15}N_{SPM}$, 54 yielded estimates of f_{new} that fell outside the range of 0–1 (gray symbols in Figures S19b and S19c in Supporting Information S1). These samples were mainly collected near the islands, the continents, and at the mouth of the Ross Sea (Figure S14 in Supporting Information S1). Here, processes such as bathymetrically induced mixing, ice melt, and/or terrestrial N inputs may have altered the mixed-layer NO_3^- and/or NH_4^+ pools (e.g., Cavagna et al., 2015; Fripiat et al., 2014; Shatova et al., 2016), violating the Rayleigh model assumption of a closed system and rendering f_{new} invalid. Mathematically, $\delta^{15}N_{SPM_{new}}$ must be higher than the measured $\delta^{15}N_{SPM}$ to produce an acceptable f_{new}; if $\delta^{15}N_{SPM_{new}} < \delta^{15}N_{SPM_{RN}}$, then $f_{new} < 0$ and if $\delta^{15}N_{SPM_{RN}} < \delta^{15}N_{SPM_{new}} < \delta^{15}N_{SPM}$, then $f_{new} > 1$ (Figure S14a in Supporting Information S1). The $\delta^{15}N_{SPM}$ at the sites where the model failed was on average 2.0 ± 2.0‰ higher than the $\delta^{15}N_{SPM_{new}}$ derived for those sites ($\delta^{15}N_{SPM} = 2.2_{0.9}^{3.3}$ and $\delta^{15}N_{SPM_{new}} = 0.8_{-0.2}^{+1.6}$‰ for $f_{new} \notin (0, 1)$) and 2.4 ± 3.5‰ higher than the $\delta^{15}N_{SPM}$ measured elsewhere ($\delta^{15}N_{SPM} = -0.5_{-1.6}^{+0.6}$‰ for $f_{new} \in (0, 1)$). These high $\delta^{15}N_{SPM}$ values likely reflect phytoplankton consumption of N sources other than subsurface NO_3^- and recycled NH_4^+, such as terrestrially derived N, which can be very high in $\delta^{15}N$ (Erskine et al., 1998; Wainright et al., 1998), and/or non-assimilation N-cycle processes such as bacterial decomposition of SPM, which raises its $\delta^{15}N$ (Möbius, 2013). Since our sampling was conducted during a period of active phytoplankton growth when SPM production would have exceeded its degradation, we suggest that the consumption of external N accounts for most of the anomalous $\delta^{15}N_{SPM}$ values.

We measured high concentrations of NH_4^+ near the islands and Antarctica (Figure 2d), which may have been partly supplied via terrestrial run-off and/or melting sea-ice and glaciers (Fripiat et al., 2014; Otero et al., 2018). Land-derived NH_4^+ is generally high in $\delta^{15}N$ due to trophic enrichment and/or volatilization of ammonia gas from guano and other organic matter deposited by sea birds and mammals (i.e., the $\delta^{15}N$ of guano can be >12‰; Mizutani et al., 1986; Wainright et al., 1998). Phytoplankton consumption of this high $\delta^{15}N_{NH_4^+}$ could yield higher values of $\delta^{15}N_{SPM}$ than is possible from the assimilation of subsurface NO_3^-.

The high $\delta^{15}N_{SPM}$ at the mouth of the Ross Sea and near Siple Island (Figure 3e) may have been influenced by the release of nutrients from melting sea-ice and/or coastal glaciers. Surface NH_4^+ concentrations were relatively high almost everywhere during Leg2 ($0.9_{0.5}^{1.3}\mu M$), particularly between the Mertz Glacier and Scott Island and downstream of Peter 1st Island (>1.5 μM) (Figure 2d). Remineralization of organic N produced by ice algae and excretion by zooplankton feeding under the sea-ice produce NH_4^+ and other reduced N forms that accumulate in and under the ice from winter to early summer (Fripiat et al., 2014, 2017; Louw et al., 2022; Roukaerts et al., 2016). This NH_4^+ appears to be relatively low in $\delta^{15}N$ (<0‰; Fripiat et al., 2014), as would be expected given the N isotope effects associated with its production (Macko et al., 1986; Möbius, 2013; Silfer et al., 1992). However, there may be times when co-occurring NH_4^+ assimilation, which occurs with little to no fractionation (Hoch et al., 1992; Liu et al., 2013; Pennock et al., 1996), and NH_4^+ oxidation, which is associated with a large isotope effect (14–19‰; Casciotti et al., 2003), cause the $\delta^{15}N$ of the sea-ice NH_4^+ pool to rise significantly. In contrast to NH_4^+, algal NO_3^- consumption is a fractionating process, which in the spring/summer sea-ice yields a relatively low-concentration NO_3^- pool that can be very high in $\delta^{15}N$ (Fripiat et al., 2014; Roukaerts et al., 2016). When the ice melts, the N species are released into the water column, along with high concentrations of iron (Lannuzel et al., 2016). This iron stimulates phytoplankton NO_3^- consumption (Timmermans et al., 1994), including of the high-$\delta^{15}N$ NO_3^- released from the ice, resulting in the production of higher $\delta^{15}N_{SPM}$ than predicted by a Rayleigh model initialized with the underlying $\delta^{15}N_{NO_3^-(source)}$.

4.2. Estimating Relative Carbon Export Potential From $\delta^{15}N_{SPM}$

In this study, we aimed to assess Southern Ocean carbon export potential by estimating the fraction of organic matter produced via the uptake of new versus regenerated nutrients (i.e., subsurface NO_3^- vs. recycled NH_4^+; Dugdale & Goering, 1967; Eppley & Peterson, 1979). The relative strength of the biological pump can be approximated by the f-ratio, assuming that the surface ocean is at steady state over an annual cycle (Eppley & Peterson, 1979). Here, we derive f_{new}, a measure of the f-ratio, using a two-endmember isotope mixing model, with the $\delta^{15}N$ of the consumed NO_3^- (i.e., $\delta^{15}N_{SPM_{new}}$) estimated via the Rayleigh model. However, instead of assuming that the $\delta^{15}N_{SPM}$ generated from the assimilation of subsurface NO_3^- can be approximated by the accumulated (or instantaneous) product equation, we account for the fact that some portion of the SPM would have been exported from the surface layer between the start of the growth season and our sampling. Above, we have discussed cases in which our isotope mixing model failed (e.g., due to an input of high-$\delta^{15}N$ allochthonous N). Below, we discuss our estimates of f_{new} and the implications for carbon export potential in the case where the $\delta^{15}N_{SPM}$ data are well described by the model (i.e., 68% of the observations).

In a mass balance sense, our data suggest that the Southern Ocean exports >40% of the carbon produced in the summer ($f_{new} = 41_{32}^{60}\%$), with minimal difference between the Subantarctic and Antarctic Oceans (39 ± 20% and 43 ± 32% [median ± IQR], respectively; Figure 8; Table 4). These values generally agree with existing estimates of the f-ratio for the summertime Southern Ocean (which averages ~50%; e.g., Joubert et al., 2011; Le Moigne et al., 2016; Mdutyana et al., 2020; Prakash et al., 2015; Sambrotto & Mace, 2000; Schlitzer, 2002). Examining our data by zone shows that f_{new} decreased by ~20% from the high to the lower latitudes (Figure 8b). In the sBZ, 60 ± 21% of phytoplankton carbon was potentially exported, reaching ~80% near the sea-ice (e.g., at the Ross Sea mouth; Table 4 and Figure 8b). f_{new} was lowest in the STZ, although ~30% of NPP was still potentially exported. Across the SAZ, PFZ, and SACCZ, f_{new} was highly variable (ranging between 7% and ~98%), yet similar median values were estimated (39%–44%). High values of f_{new} (>65%) were associated with stations near and downstream of many of the islands, with ~75% of NPP potentially exported near the PEIs and >80% downstream of Kerguelen Island. Lower values of f_{new} (<50%) were determined for open ocean stations that were distant from the islands or covered with sea-ice (e.g., the open STZ, south of Tasmania, and the SACCZ during the latter half of Leg2; Figure 8a). The apparent latitudinal trend in f_{new} may thus be driven principally by processes that occur at

the regional scale, such as the alleviation of iron limitation that leads to proportionally higher NO_3^- dependence near the islands, at the hydrographic fronts, and off the continental shelves. For instance, the large region between the South Sandwich and Bouvet Islands that was characterized by a high f_{new} (73 ± 33%) may have biased the mean SACCZ estimate upwards, while most of the truly open ocean stations where regenerated production dominated were located at lower latitudes, potentially biasing those f_{new} estimates downwards.

NO_3^- uptake by Southern Ocean phytoplankton is typically enhanced by an increase in light, a stable upper water column, and an input of limiting nutrients (i.e., iron and/or SiO_4^{4-}) via upwelling, terrestrial run-off, and/or melting sea-ice and glaciers (Cochlan, 2008 and references therein). The island mass effect is generally associated with upwelling, input of land-derived nutrients, and retention and stabilization of surface waters over shallow plateaus, which drive localized increases in phytoplankton biomass and nutrient and CO_2 drawdown (e.g., Holmes et al., 2019; Planquette et al., 2011; Schallenberg et al., 2018). In the Ross Sea, large and persistent polynyas reduce sea-ice cover, increasing stratification and light (Arrigo et al., 2015; Gordon et al., 2000), as well as iron availability (Alderkamp et al., 2012). Relief from iron limitation enhances NO_3^- reductase activity in phytoplankton, particularly diatoms, allowing for higher NO_3^- uptake and increased rates of biomass production (Blain et al., 2007; De Baar et al., 1997; Karsh et al., 2003; Timmermans et al., 1994). By contrast, low iron concentrations limit NO_3^- uptake and favor the growth of small phytoplankton reliant on regenerated N (Martin et al., 1990; Sunda & Hardison, 2007). In our dataset, the open ocean regions were characterized by low iron concentrations (<0.05 nmol kg^{-1}; Figure 2e) and supported low biomass and a higher proportion of nano-phytoplankton, predominantly haptophytes (Figure 5d; Text S6 in Supporting Information S1), which may be more efficient than diatoms at utilizing bacterially regenerated iron (Fourquez et al., 2022). By contrast, near the South Sandwich Islands, PEIs, and Heard Island, iron concentrations were higher (≥0.2 nmol kg^{-1}), biomass and micro-phytoplankton contributions to total Chl-a were elevated, large diatoms were abundant (Figures 5e and 7), and local minima were observed in pCO_2 (Figure 2f). Interestingly, downstream of Crozet Island (50–60°E), the plankton assemblage was dominated by nano-phytoplankton (mainly haptophytes) and diatom abundance was low; here, regenerated N fueled more than half of NPP, limiting carbon export potential.

Between Siple Island and the Drake Passage, biomass and f_{new} were notably low (Figures 5a and 8b) and the NH_4^+ concentrations were high (0.9–2 μM; Figure 2d). Near melting sea-ice, the specific rates of NO_3^- and NH_4^+ uptake have been observed to correlate positively with their respective concentrations (R. Zhang et al., 2019). Thus, high NH_4^+ concentrations supplied by melting sea-ice (Fripiat et al., 2014; Roukaerts et al., 2016) could underpin the low values of f_{new}. At the same time, a large increase in NH_4^+ availability in regions with high dissolved iron and low NH_4^+ concentrations can both enhance NH_4^+ uptake and (partly) inhibit NO_3^- consumption by phytoplankton (Elskens et al., 2002).

Across the Southern Ocean, f_{new} was slightly positively correlated with SiO_4^{4-} (ρ = +0.25, p-value <0.001; Figure S16 in Supporting Information S1). Since the availability of SiO_4^{4-} controls the distribution of diatoms (Hoffmann et al., 2008) that typically dominate new production (Dugdale et al., 1995; Egge & Aksnes, 1992), and given that the fraction of micro-phytoplankton was strongly positively correlated with SiO_4^{4-} (ρ = +0.70, p-value <0.001), the relationship of f_{new} to SiO_4^{4-} is not unexpected. Consistently, f_{new} was also positively correlated with micro-phytoplankton biomass, weakly in the Subantarctic and strongly in the Antarctic (ρ = +0.28 and + 0.56, respectively; Figures S17, S18, and S20 in Supporting Information S1). By contrast, low values of f_{new} occurred where nano-phytoplankton (mainly haptophytes) dominated, typically in open ocean waters. Here, low iron availability limits diatom growth and NO_3^- assimilation (Timmermans et al., 2004), which leads to the development of regenerated N-fueled systems dominated by nano-phytoplankton that are more competitive for scarce nutrients (Fourquez et al., 2022; Hare et al., 2007).

5. Conclusions

In this circum-Antarctic study, we sought to (a) better understand the drivers of $\delta^{13}C_{SPM}$ and $\delta^{15}N_{SPM}$ isoscape variability across the summertime Southern Ocean and (b) quantify carbon export potential from measurements of $\delta^{15}N_{SPM}$. In general, the latitudinal gradients in $\delta^{13}C_{SPM}$ and $\delta^{15}N_{SPM}$ were consistent with previous studies, with clear differences observed between the Subantarctic and Antarctic Oceans. As expected, $\delta^{13}C_{SPM}$ was highly dependent on seawater pCO_2, with phytoplankton community composition helping to explain values of $\delta^{13}C_{SPM}$ that deviated from the expected relationship with pCO_2. The observed trends in $\delta^{15}N_{SPM}$ were driven by the $\delta^{15}N$ of the N nutrients and the extent of phytoplankton reliance on new versus regenerated N. Phytoplankton

community composition also played a role as some taxa specialize in NO_3^- assimilation while others favor recycled NH_4^+ consumption. In contrast to previous isoscape studies, this work highlights the considerable influence of phytoplankton community dynamics on $\delta^{13}C_{SPM}$ and $\delta^{15}N_{SPM}$. For instance, higher $\delta^{13}C_{SPM}$ was linked to higher haptophyte abundance, and is thus potentially explained by their carboxylation of HCO_3^- using PEPc. Conversely, higher $\delta^{15}N_{SPM}$ usually coincided with a greater contribution to the phytoplankton assemblage of diatoms, which specialize in the assimilation of NO_3^-.

We employed a novel approach to determine relative carbon export potential using a two-endmember isotope mixing model that incorporated the Rayleigh equations for isotope fractionation during NO_3^- assimilation by phytoplankton. Our derived values of f_{new} are consistent with previous summertime measurements of the f-ratio, which validates our approach, although we note that different methods for estimating the f-ratio integrate over different time scales, making a direct comparison difficult. For example, f-ratios determined from ^{15}N-tracer-based measurements of NO_3^- and NH_4^+ uptake (e.g., Joubert et al., 2011; Mdutyana et al., 2020) reflect the conditions of the water column at the time of sampling while our $\delta^{15}N_{SPM}$-based approach integrates over weeks to months, and geochemical estimates (e.g., profiling float-based measurements of NO_3^- consumption; Johnson et al., 2017) can integrate over the annual cycle. We estimate that on average, >40% of the carbon produced in Southern Ocean surface waters was potentially exported, with a higher percentage near the (Sub)Antarctic islands and in regions of melting sea-ice, induced by an increase in phytoplankton growth rates and NO_3^- uptake, likely in response to iron input. The onset of iron limitation should drive phytoplankton to consume proportionally more NH_4^+ as the growth season progresses (Cochlan, 2008; Smith et al., 2022). As such, f_{new} is likely to have declined following our sampling. By the same logic, however, f_{new} would have been considerably higher at the beginning of the growth season, with much of the organic N then produced already exported by the time of our sampling. We thus conclude that our estimates of f_{new} provide a reasonable approximation of the fraction of NPP exported from the Southern Ocean surface during the summer growth period.

Bulk SPM is easily sampled and $\delta^{13}C_{SPM}$ and $\delta^{15}N_{SPM}$ are already widely analyzed. Here we show how $\delta^{15}N_{SPM}$ can be used to infer relative carbon export potential, an approach that could be applied to other ocean regions. We find that $\delta^{15}N_{NO_3^-(source)}$ is a critical variable that should be measured alongside $\delta^{15}N_{SPM}$; indeed, $\delta^{15}N_{NO_3^-(source)}$ varies by >3‰ across the Southern Ocean, meaning that 3‰ of the variability in $\delta^{15}N_{SPM}$ could be explained by NO_3^- $\delta^{15}N$ alone, before changes in new versus regenerated N uptake or phytoplankton community dynamics need to be invoked. As such, we recommend that studies using measurements of $\delta^{15}N_{SPM}$ (e.g., trophic analyses) consider the influence of $\delta^{15}N_{NO_3^-(source)}$.

Data Availability Statement

The metadata supporting the conclusions of this article, which utilizes the two-endmember model, can be found as Stirnimann and Fawcett (2023), available under the https://doi.org/10.5281/zenodo.8422942.

References

Alderkamp, A.-C., Mills, M. M., van Dijken, G. L., Laan, P., Thuróczy, C.-E., Gerringa, L. J. A., et al. (2012). Iron from melting glaciers fuels phytoplankton blooms in the Amundsen Sea (Southern Ocean): Phytoplankton characteristics and productivity. *Deep Sea Research Part II: Topical Studies in Oceanography*, *71–76*, 32–48. https://doi.org/10.1016/j.dsr2.2012.03.005

Altabet, M. A. (1988). Variations in nitrogen isotopic composition between sinking and suspended particles: Implications for nitrogen cycling and particle transformation in the open ocean. *Deep-Sea Research, Part A: Oceanographic Research Papers*, *35*(4), 535–554. https://doi.org/10.1016/0198-0149(88)90130-6

Altabet, M. A., & Francois, R. (1994). Sedimentary nitrogen isotopic ratio as a recorder for surface ocean nitrate utilization. *Global Biogeochemical Cycles*, *8*(1), 103–116. https://doi.org/10.1029/93GB03396

Altabet, M. A., & Francois, R. (2001). Nitrogen isotope biogeochemistry of the Antarctic Polar Frontal Zone at 170°W. *Deep Sea Research Part II: Topical Studies in Oceanography*, *48*(19), 4247–4273. https://doi.org/10.1016/S0967-0645(01)00088-1

Antoine, D., Thomalla, S., Berliner, D., Little, H., Moutier, W., Olivier-Morgan, A., et al. (2020). Phytoplankton pigment concentrations of seawater sampled during the Antarctic Circumnavigation Expedition (ACE) during the Austral Summer of 2016/2017. (1.1) [Dataset]. https://zenodo.org/records/3406983

Arnelle, D. R., & O'Leary, M. H. (1992). Binding of carbon dioxide to phosphoenolpyruvate carboxykinase deduced from carbon kinetic isotope effects. *Biochemistry*, *31*(17), 4363–4368. https://doi.org/10.1021/bi00132a029

Arrigo, K. R., van Dijken, G., & Long, M. (2008). Coastal Southern Ocean: A strong anthropogenic CO_2 sink. *Geophysical Research Letters*, *35*(21). https://doi.org/10.1029/2008GL035624

Arrigo, K. R., van Dijken, G. L., & Bushinsky, S. (2008). Primary production in the Southern Ocean, 1997–2006. *Journal of Geophysical Research*, *113*(C8). https://doi.org/10.1029/2007JC004551

Arrigo, K. R., van Dijken, G. L., & Strong, A. L. (2015). Environmental controls of marine productivity hot spots around Antarctica. *Journal of Geophysical Research: Oceans*, *120*(8), 5545–5565. https://doi.org/10.1002/2015JC010888

Arteaga, L., Haëntjens, N., Boss, E., Johnson, K. S., & Sarmiento, J. L. (2018). Assessment of export efficiency equations in the Southern Ocean applied to satellite-based net primary production. *Journal of Geophysical Research: Oceans*, *123*(4), 2945–2964. https://doi.org/10.1002/2018JC013787

Berg, G. M., Mills, M. M., Long, M. C., Bellerby, R., Strass, V., Savoye, N., et al. (2011). Variation in particulate C and N isotope composition following iron fertilization in two successive phytoplankton communities in the Southern Ocean. *Global Biogeochemical Cycles*, *25*(3). https://doi.org/10.1029/2010GB003824

Blain, S., Quéguiner, B., Armand, L., Belviso, S., Bombled, B., Bopp, L., et al. (2007). Effect of natural iron fertilization on carbon sequestration in the Southern Ocean. *Nature*, *446*(7139), 1070–1074. https://doi.org/10.1038/nature05700

Bowen, G. J. (2010). Isoscapes: Spatial pattern in isotopic biogeochemistry. *Annual Review of Earth and Planetary Sciences*, *38*(1), 161–187. https://doi.org/10.1146/annurev-earth-040809-152429

Bowie, A. R., Brian Griffiths, F., Dehairs, F., & Trull, T. W. (2011). Oceanography of the subantarctic and Polar Frontal Zones south of Australia during summer: Setting for the SAZ-sense study. *Deep Sea Research Part II: Topical Studies in Oceanography*, *58*(21), 2059–2070. https://doi.org/10.1016/j.dsr2.2011.05.033

Brault, E., Koch, P., McMahon, K., Broach, K., Rosenfield, A. P., Sauthoff, W., et al. (2018). Carbon and nitrogen zooplankton isoscapes in West Antarctica reflect oceanographic transitions. *Marine Ecology Progress Series*, *593*, 29–45. https://doi.org/10.3354/meps12524

Casciotti, K. L., Sigman, D. M., & Ward, B. B. (2003). Linking diversity and stable isotope fractionation in ammonia-oxidizing bacteria. *Geomicrobiology Journal*, *20*(4), 335–353. https://doi.org/10.1080/01490450303895

Cavagna, A. J., Fripiat, F., Elskens, M., Mangion, P., Chirurgien, L., Closset, I., et al. (2015). Production regime and associated N cycling in the vicinity of Kerguelen Island, Southern Ocean. *Biogeosciences*, *12*(21), 6515–6528. https://doi.org/10.5194/bg-12-6515-2015

Checkley, D. M., & Miller, C. A. (1989). Nitrogen isotope fractionation by oceanic zooplankton. *Deep-Sea Research, Part A: Oceanographic Research Papers*, *36*(10), 1449–1456. https://doi.org/10.1016/0198-0149(89)90050-2

Chen, S.-Y., Feng, Z., & Yi, X. (2017). A general introduction to adjustment for multiple comparisons. *Journal of Thoracic Disease*, *9*(6), 1725–1729. https://doi.org/10.21037/jtd.2017.05.34

Cochlan, W. P. (2008). Nitrogen uptake in the Southern Ocean. In D. G. Capone, D. A. Bronk, M. R. Mulholland, & E. J. Carpenter (Eds.), *Nitrogen in the marine environment* (2nd ed., pp. 569–596). Academic Press, Elsevier.

Death, R., Wadham, J. L., Monteiro, F., Le Brocq, A. M., Tranter, M., Ridgwell, A., et al. (2014). Antarctic ice sheet fertilises the Southern Ocean. *Biogeosciences*, *11*(10), 2635–2643. https://doi.org/10.5194/bg-11-2635-2014

De Baar, H. J. W., Van Leeuwe, M. A., Scharek, R., Goeyens, L., Bakker, K. M. J., & Fritsche, P. (1997). Nutrient anomalies in *Fragilariopsis kerguelensis* blooms, iron deficiency and the nitrate/phosphate ratio (A. C. Redfield) of the Antarctic Ocean. *Deep Sea Research Part II: Topical Studies in Oceanography*, *44*(1), 229–260. https://doi.org/10.1016/S0967-0645(96)00102-6

De Falco, C., Desbiolles, F., Bracco, A., & Pasquero, C. (2022). Island mass effect: A review of oceanic physical processes. *Frontiers in Marine Science*, *1252*. https://doi.org/10.3389/fmars.2022.894860

Descolas-Gros, C., & Fontugne, M. (1990). Stable carbon isotope fractionation by marine phytoplankton during photosynthesis. *Plant, Cell and Environment*, *13*(3), 207–218. https://doi.org/10.1111/j.1365-3040.1990.tb01305.x

Descolas-Gros, C., & Fontugne, M. R. (1985). Carbon fixation in marine phytoplankton: Carboxylase activities and stable carbon-isotope ratios; physiological and paleoclimatological aspects. *Marine Biology*, *87*(1), 1–6. https://doi.org/10.1007/bf00396999

Descolas-Gros, C., & Oriol, L. (1992). Variations in carboxylase activity in marine phytoplankton cultures. β-carboxylation in carbon flux studies. *Marine Ecology Progress Series*, *85*(1/2), 163–169. https://doi.org/10.3354/meps085163

Deuser, W. G. (1970). Isotopic evidence for diminishing supply of available carbon during diatom bloom in the black sea. *Nature*, *225*(5237), 1069–1071. https://doi.org/10.1038/2251069a0

DeVries, T. (2014). The oceanic anthropogenic CO_2 sink: Storage, air-sea fluxes, and transports over the industrial era. *Global Biogeochemical Cycles*, *28*(7), 631–647. https://doi.org/10.1002/2013GB004739

Diamond, D. (1994). *QuikChem Method 10-114-21-1-B: Silicate by flow injection analysis*. Lachat Instruments.

DiFiore, P. J., Sigman, D. M., Karsh, K. L., Trull, T. W., Dunbar, R. B., & Robinson, R. S. (2010). Poleward decrease in the isotope effect of nitrate assimilation across the Southern Ocean. *Geophysical Research Letters*, *37*(17). https://doi.org/10.1029/2010GL044090

Dugdale, R. C., & Goering, J. J. (1967). Uptake of new and regenerated forms of nitrogen in primary productivity. *Limnology & Oceanography*, *12*(2), 196–206. https://doi.org/10.4319/lo.1967.12.2.0196

Dugdale, R. C., Wilkerson, F. P., & Minas, H. J. (1995). The role of a silicate pump in driving new production. *Deep Sea Research Part I: Oceanographic Research Papers*, *42*(5), 697–719. https://doi.org/10.1016/0967-0637(95)00015-X

Egge, J. K., & Aksnes, D. L. (1992). Silicate as regulating nutrient in phytoplankton competition. *Marine Ecology Progress Series. Oldendorf*, *83*(2), 281–289. https://doi.org/10.3354/meps083281

Elskens, M., Baeyens, W., Cattaldo, T., Dehairs, F., & Griffiths, B. (2002). N uptake conditions during summer in the Subantarctic and Polar Frontal Zones of the Australian sector of the Southern Ocean. *Journal of Geophysical Research*, *107*(C11), 3–11. https://doi.org/10.1029/2001JC000897

Eppley, R. W., & Peterson, B. J. (1979). Particulate organic matter flux and planktonic new production in the deep ocean. *Nature*, *282*(5740), 677–680. https://doi.org/10.1038/282677a0

Eppley, R. W., Rogers, J. N., & McCarthy, J. J. (1969). Half-saturation constants for uptake of nitrate and ammonium by marine phytoplankton 1. *Limnology & Oceanography*, *14*(6), 912–920. https://doi.org/10.4319/lo.1969.14.6.0912

Erskine, P. D., Bergstrom, D. M., Schmidt, S., Stewart, G. R., Tweedie, C. E., & Shaw, J. D. (1998). Subantarctic Macquarie Island – A model ecosystem for studying animal-derived nitrogen sources using ^{15}N natural abundance. *Oecologia*, *117*(1), 187–193. https://doi.org/10.1007/s004420050647

Espinasse, B., Pakhomov, E., Hunt, B. P. V., & Bury, S. (2019). Latitudinal gradient consistency in carbon and nitrogen stable isotopes of particulate organic matter in the Southern Ocean. *Marine Ecology Progress Series*, *631*, 19–30. https://doi.org/10.3354/meps13137

Falkowski, P. G. (1991). Species variability in the fractionation of ^{13}C and ^{12}C by marine phytoplankton. *Journal of Plankton Research*, *13*(supp1), 21–28. https://doi.org/10.1093/oxfordjournals.plankt.a042367

Falkowski, P. G., Barber, R. T., & Smetacek, V. (1998). Biogeochemical controls and feedbacks on ocean primary production. *Science*, *281*(5374), 200–206. https://doi.org/10.1126/science.281.5374.200

Fan, G., Han, Z., Ma, W., Chen, S., Chai, F., Mazloff, M. R., et al. (2020). Southern Ocean carbon export efficiency in relation to temperature and primary productivity. *Scientific Reports*, *10*(1), 13494. https://doi.org/10.1038/s41598-020-70417-z

Fawcett, S. E., Lomas, M. W., Casey, J. R., Ward, B. B., & Sigman, D. M. (2011). Assimilation of upwelled nitrate by small eukaryotes in the Sargasso Sea. *Nature Geoscience*, *4*(10), 717–722. https://doi.org/10.1038/ngeo1265

Fawcett, S. E., Lomas, M. W., Ward, B. B., & Sigman, D. M. (2014). The counterintuitive effect of summer-to-fall mixed layer deepening on eukaryotic new production in the Sargasso Sea. *Global Biogeochemical Cycles*, *28*(2), 86–102. https://doi.org/10.1002/2013GB004579

Flynn, R. F. (2023). *Phytoplankton's role in the biological pump during the growth season across the Atlantic Southern Ocean*. (Unpublished PhD Dissertation). Faculty of Science, Department of Oceanography, University of Cape Town.

Fourquez, M., Strzepek, R. F., Ellwood, M. J., Hassler, C., Cabanes, D., Eggins, S., et al. (2022). Phytoplankton responses to bacterially regenerated iron in a Southern Ocean Eddy. *Microorganisms*, *10*(8), 1655. https://doi.org/10.3390/microorganisms10081655

François, R., Altabet, M. A., Goericke, R., McCorkle, D. C., Brunet, C., & Poisson, A. (1993). Changes in the $\delta^{13}C$ of surface water particulate organic matter across the subtropical convergence in the SW Indian Ocean. *Global Biogeochemical Cycles*, *7*(3), 627–644. https://doi.org/10.1029/93GB01277

Fransson, A., Chierici, M., Yager, P. L., & Smith, W. O., Jr. (2011). Antarctic sea ice carbon dioxide system and controls. *Journal of Geophysical Research*, *116*(C12), C12035. https://doi.org/10.1029/2010JC006844

Freeman, K. H., & Hayes, J. M. (1992). Fractionation of carbon isotopes by phytoplankton and estimates of ancient CO_2 levels. *Global Biogeochemical Cycles*, *6*(2), 185–198. https://doi.org/10.1029/92GB00190

Fripiat, F., Marconi, D., Rafter, P. A., Sigman, D. M., Altabet, M. A., Bourbonnais, A., et al. (2021). Compilation of nitrate $\delta^{15}N$ in the ocean. *PANGAEA*. https://doi.org/10.1594/PANGAEA.936484

Fripiat, F., Martínez-García, A., Fawcett, S. E., Kemeny, P. C., Studer, A. S., Smart, S. M., et al. (2019). The isotope effect of nitrate assimilation in the Antarctic Zone: Improved estimates and paleoceanographic implications. *Geochimica et Cosmochimica Acta*, *247*, 261–279. https://doi.org/10.1016/j.gca.2018.12.003

Fripiat, F., Meiners, K. M., Vancoppenolle, M., Papadimitriou, S., Thomas, D. N., Ackley, S. F., et al. (2017). Macro-nutrient concentrations in Antarctic pack ice: Overall patterns and overlooked processes. *Elementa: Science of the Anthropocene*, *5*, 13. https://doi.org/10.1525/elementa.217

Fripiat, F., Sigman, D. M., Fawcett, S. E., Rafter, P. A., Weigand, M. A., & Tison, J.-L. (2014). New insights into sea ice nitrogen biogeochemical dynamics from the nitrogen isotopes. *Global Biogeochemical Cycles*, *28*(2), 115–130. https://doi.org/10.1002/2013GB004729

Frölicher, T. L., Sarmiento, J. L., Paynter, D. J., Dunne, J. P., Krasting, J. P., & Winton, M. (2015). Dominance of the Southern Ocean in anthropogenic carbon and heat uptake in CMIP5 models. *Journal of Climate*, *28*(2), 862–886. https://doi.org/10.1175/jcli-d-14-00117.1

Fry, B., & Sherr, E. B. (1989). $\delta^{13}C$ measurements as indicators of carbon flow in marine and freshwater ecosystems. In P. W. Rundel, J. R. Ehleringer, & K. A. Nagy (Eds.), *Stable isotopes in ecological research. Ecological studies* (Vol. 68, pp. 196–229). Springer. https://doi.org/10.1007/978-1-4612-3498-2_12

Fry, B., & Wainright, S. C. (1991). Diatom sources of ^{13}C-rich carbon in marine food webs. *Marine Ecology Progress Series*, *76*–149. https://doi.org/10.3354/meps076149

Garcia, N. S., Sexton, J., Riggins, T., Brown, J., Lomas, M. W., & Martiny, A. C. (2018). High variability in cellular stoichiometry of carbon, nitrogen, and phosphorus within classes of marine eukaryotic phytoplankton under sufficient nutrient conditions. *Frontiers in Microbiology*, *9*. https://doi.org/10.3389/fmicb.2018.00543

Goericke, R. (1994). Physiology of isotopic fractionation in algae and cyanobacteria. *Stable Isotopes in Ecology and Environmental Science*, 187–221.

Gordon, L. I., Codispoti, L. A., Jennings, J. C., Millero, F. J., Morrison, J. M., & Sweeney, C. (2000). Seasonal evolution of hydrographic properties in the Ross Sea, Antarctica, 1996–1997. *Deep Sea Research Part II: Topical Studies in Oceanography*, *47*(15), 3095–3117. https://doi.org/10.1016/S0967-0645(00)00060-6

Granger, J., Sigman, D. M., Needoba, J. A., & Harrison, P. J. (2004). Coupled nitrogen and oxygen isotope fractionation of nitrate during assimilation by cultures of marine phytoplankton. *Limnology & Oceanography*, *49*(5), 1763–1773. https://doi.org/10.4319/lo.2004.49.5.1763

Grasshoff, K. (1976). Automated chemical analysis. *Methods of Seawater Analysis*, 263–297.

Gruber, N., Keeling, C. D., Bacastow, R. B., Guenther, P. R., Lueker, T. J., Wahlen, M., et al. (1999). Spatiotemporal patterns of carbon-13 in the global surface oceans and the oceanic Suess effect. *Global Biogeochemical Cycles*, *13*(2), 307–335. https://doi.org/10.1029/1999GB900019

Guy, R. D., Vanlerberghe, G. C., & Turpin, D. H. (1989). Significance of phosphoenolpyruvate carboxylase during ammonium assimilation: Carbon isotope discrimination in photosynthesis and respiration by the N-limited green Alga *Selenastrum minutum* 1. *Plant Physiology*, *89*(4), 1150–1157. https://doi.org/10.1104/pp.89.4.1150

Hare, C. E., DiTullio, G. R., Riseman, S. F., Crossley, A. C., Popels, L. C., Sedwick, P. N., & Hutchins, D. A. (2007). Effects of changing continuous iron input rates on a Southern Ocean algal assemblage. *Deep Sea Research Part I: Oceanographic Research Papers*, *54*(5), 732–746. https://doi.org/10.1016/j.dsr.2007.02.001

Hassler, C., & Ellwood, M. (2020). Nutrient concentration in seawater samples, collected from the underway supply, CTD and trace metal rosettes in the Southern Ocean during the austral summer of 2016/2017, on board the Antarctic Circumnavigation Expedition (ACE). (Version 1.1) [Dataset]. Zenodo. https://doi.org/10.5281/zenodo.3923586

Henley, S. F., Cavan, E. L., Fawcett, S. E., Kerr, R., Monteiro, T., Sherrell, R. M., et al. (2020). Changing biogeochemistry of the Southern Ocean and its ecosystem implications. *Frontiers in Marine Science*, *7*. https://doi.org/10.3389/fmars.2020.00581

Hildebrand, M., & Dahlin, K. (2000). Nitrate transporter genes from the diatom *Cylindrotheca fusiformis* (Bacillariophyceae): mRNA levels controlled by nitrogen source and by the cell cycle. *Journal of Phycology*, *36*(4), 702–713. https://doi.org/10.1046/j.1529-8817.2000.99153.x

Hirawake, T., Takao, S., Horimoto, N., Ishimaru, T., Yamaguchi, Y., & Fukuchi, M. (2011). A phytoplankton absorption-based primary productivity model for remote sensing in the Southern Ocean. *Polar Biology*, *34*(2), 291–302. https://doi.org/10.1007/s00300-010-0949-y

Hoch, M. P., Fogel, M. L., & Kirchman, D. L. (1992). Isotope fractionation associated with ammonium uptake by a marine bacterium. *Limnology & Oceanography*, *37*(7), 1447–1459. https://doi.org/10.4319/lo.1992.37.7.1447

Hoffmann, L. J., Peeken, I., & Lochte, K. (2008). Iron, silicate, and light co-limitation of three Southern Ocean diatom species. *Polar Biology*, *31*(9), 1067–1080. https://doi.org/10.1007/s00300-008-0448-6

Holmes, T. M., Wuttig, K., Chase, Z., van der Merwe, P., Townsend, A. T., Schallenberg, C., et al. (2019). Iron availability influences nutrient drawdown in the Heard and McDonald Islands region, Southern Ocean. *Marine Chemistry*, *211*(February), 1–14. https://doi.org/10.1016/j.marchem.2019.03.002

Janssen, D. J., Sieber, M., Ellwood, M. J., Conway, T. M., Barrett, P. M., Chen, X., et al. (2020). Trace metal and nutrient dynamics across broad biogeochemical gradients in the Indian and Pacific sectors of the Southern Ocean. *Marine Chemistry*, *221*, 103773. https://doi.org/10.1016/j.marchem.2020.103773

Jena, B. (2016). Satellite remote sensing of the island mass effect on the Sub-Antarctic Kerguelen plateau, Southern Ocean. *Frontiers of Earth Science*, *10*(3), 479–486. https://doi.org/10.1007/s11707-016-0561-8

Johnson, K. S., Plant, J. N., Dunne, J. P., Talley, L. D., & Sarmiento, J. L. (2017). Annual nitrate drawdown observed by SOCCOM profiling floats and the relationship to annual net community production. *Journal of Geophysical Research: Oceans*, *122*(8), 6668–6683. https://doi.org/10.1002/2017JC012839

Joubert, W. R., Thomalla, S. J., Waldron, H. N., Lucas, M. I., Boye, M., Le Moigne, F. A. C., et al. (2011). Nitrogen uptake by phytoplankton in the Atlantic sector of the Southern Ocean during late austral summer. *Biogeosciences*, *8*(10), 2947–2959. https://doi.org/10.5194/bg-8-2947-2011

Karsh, K. L., Trull, T. W., Lourey, M. J., & Sigman, D. M. (2003). Relationship of nitrogen isotope fractionation to phytoplankton size and iron availability during the Southern Ocean Iron RElease Experiment (SOIREE). *Limnology & Oceanography*, *48*(3), 1058–1068. https://doi.org/10.4319/lo.2003.48.3.1058

Kerkar, A. U., Tripathy, S. C., Minu, P., Baranval, N., Sabu, P., Patra, S., et al. (2020). Variability in primary productivity and bio-optical properties in the Indian sector of the Southern Ocean during an austral summer. *Polar Biology*, *43*(10), 1469–1492. https://doi.org/10.1007/s00300-020-02722-2

Kroopnick, P. M. (1985). The distribution of 13C of ΣCO$_2$ in the world oceans. *Deep-Sea Research, Part A: Oceanographic Research Papers*, *32*(1), 57–84. https://doi.org/10.1016/0198-0149(85)90017-2

Landwehr, S., Volpi, M., Haumann, F. A., Robinson, C. M., Thurnherr, I., Ferracci, V., et al. (2021). Exploring the coupled ocean and atmosphere system with a data science approach applied to observations from the Antarctic Circumnavigation Expedition. *Earth System Dynamics*, *12*(4), 1295–1369. https://doi.org/10.5194/esd-12-1295-2021

Lannuzel, D., Vancoppenolle, M., van der Merwe, P., de Jong, J., Meiners, K. M., Grotti, M., et al. (2016). Iron in sea ice: Review and new insights. *Elementa: Science of the Anthropocene*, *4*, 130. https://doi.org/10.12952/journal.elementa.000130

Laws, E. A., Popp, B. N., Bidigare, R. R., Kennicutt, M. C., & Macko, S. A. (1995). Dependence of phytoplankton carbon isotopic composition on growth rate and [CO$_2$]$_{aq}$: Theoretical considerations and experimental results. *Geochimica et Cosmochimica Acta*, *59*(6), 1131–1138. https://doi.org/10.1016/0016-7037(95)00030-4

Le Moigne, F. A. C., Henson, S. A., Cavan, E., Georges, C., Pabortsava, K., Achterberg, E. P., et al. (2016). What causes the inverse relationship between primary production and export efficiency in the Southern Ocean? *Geophysical Research Letters*, *43*(9), 4457–4466. https://doi.org/10.1002/2016GL068480

Liu, K.-K., Kao, S.-J., Chiang, K.-P., Gong, G.-C., Chang, J., Cheng, J.-S., & Lan, C.-Y. (2013). Concentration dependent nitrogen isotope fractionation during ammonium uptake by phytoplankton under an algal bloom condition in the Danshuei estuary, northern Taiwan. *Marine Chemistry*, *157*, 242–252. https://doi.org/10.1016/j.marchem.2013.10.005

Lomas, M. W., & Glibert, P. M. (1999). Temperature regulation of nitrate uptake: A novel hypothesis about nitrate uptake and reduction in cool-water diatoms. *Limnology & Oceanography*, *44*(3), 556–572. https://doi.org/10.4319/lo.1999.44.3.0556

Lomas, M. W., & Glibert, P. M. (2000). Comparisons of nitrate uptake, storage, and reduction in marine diatoms and flagellates. *Journal of Phycology*, *36*(5), 903–913. https://doi.org/10.1046/j.1529-8817.2000.99029.x

Lourey, M. J., Trull, T. W., & Sigman, D. M. (2003). Sensitivity of δ^{15}N of nitrate, surface suspended and deep sinking particulate nitrogen to seasonal nitrate depletion in the Southern Ocean. *Global Biogeochemical Cycles*, *17*(3). https://doi.org/10.1029/2002GB001973

Louw, D. V. S., Walker, D. R., & Fawcett, S. E. (2022). Factors influencing sea-ice algae abundance, community composition, and distribution in the marginal ice zone of the Southern Ocean during winter. *Deep Sea Research Part I: Oceanographic Research Papers*, *185*, 103805. https://doi.org/10.1016/j.dsr.2022.103805

Mackey, M. D., Mackey, D. J., Higgins, H. W., & Wright, S. W. (1996). CHEMTAX-A program for estimating class abundances from chemical markers: Application to HPLC measurements of phytoplankton. *Marine Ecology Progress Series*, *144*, 265–283. https://doi.org/10.3354/meps144265

Macko, S. A., Estep, M. L. F., Engel, M. H., & Hare, P. E. (1986). Kinetic fractionation of stable nitrogen isotopes during amino acid transamination. *Geochimica et Cosmochimica Acta*, *50*(10), 2143–2146. https://doi.org/10.1016/0016-7037(86)90068-2

Marañón, E. (2015). Cell size as a key determinant of phytoplankton metabolism and community structure. *Annual Review of Marine Science*, *7*(1), 241–264. https://doi.org/10.1146/annurev-marine-010814-015955

Mariotti, A., Germon, J. C., Hubert, P., Kaiser, P., Letolle, R., Tardieux, A., & Tardieux, P. (1981). Experimental determination of nitrogen kinetic isotope fractionation: Some principles; illustration for the denitrification and nitrification processes. *Plant and Soil*, *62*(3), 413–430. https://doi.org/10.1007/BF02374138

Martin, J. H., Fitzwater, S. E., & Gordon, R. M. (1990). Iron deficiency limits phytoplankton growth in Antarctic waters. *Global Biogeochemical Cycles*, *4*(1), 5–12. https://doi.org/10.1029/GB004i001p00005

Mazloff, M. R., Heimbach, P., & Wunsch, C. (2010). An Eddy-permitting Southern Ocean State estimate. *Journal of Physical Oceanography*, *40*(5), 880–899. https://doi.org/10.1175/2009JPO4236.1

McCorkle, D. C., Emerson, S. R., & Quay, P. D. (1985). Stable carbon isotopes in marine porewaters. *Earth and Planetary Science Letters*, *74*(1), 13–26. https://doi.org/10.1016/0012-821X(85)90162-1

Mdutyana, M., Thomalla, S. J., Philibert, R., Ward, B. B., & Fawcett, S. E. (2020). The seasonal cycle of nitrogen uptake and nitrification in the Atlantic sector of the Southern Ocean. *Global Biogeochemical Cycles*, *34*(7), e2019GB006363. https://doi.org/10.1029/2019GB006363

Mizutani, H., Hasegawa, H., & Wada, E. (1986). High nitrogen isotope ratio for soils of seabird rookeries. *Biogeochemistry*, *2*(3), 221–247. https://doi.org/10.1007/bf02180160

Möbius, J. (2013). Isotope fractionation during nitrogen remineralization (ammonification): Implications for nitrogen isotope biogeochemistry. *Geochimica et Cosmochimica Acta*, *105*, 422–432. https://doi.org/10.1016/j.gca.2012.11.048

Mongin, M. M., Abraham, E. R., & Trull, T. W. (2009). Winter advection of iron can explain the summer phytoplankton bloom that extends 1000 km downstream of the Kerguelen Plateau in the Southern Ocean. *Journal of Marine Research*, *67*(2), 225–237. https://doi.org/10.1357/002224009789051218

Mongin, M. M., Molina, E., & Trull, T. W. (2008). Seasonality and scale of the Kerguelen plateau phytoplankton bloom: A remote sensing and modeling analysis of the influence of natural iron fertilization in the Southern Ocean. *Deep Sea Research Part II: Topical Studies in Oceanography*, *55*(5), 880–892. https://doi.org/10.1016/j.dsr2.2007.12.039

Mook, W. G., Bommerson, J. C., & Staverman, W. H. (1974). Carbon isotope fractionation between dissolved bicarbonate and gaseous carbon dioxide. *Earth and Planetary Science Letters*, *22*(2), 169–176. https://doi.org/10.1016/0012-821X(74)90078-8

Nakatsuka, T., Handa, N., Wada, E., & Wong, C. S. (1992). The dynamic changes of stable isotopic ratios of carbon and nitrogen in suspended and sedimented particulate organic matter during a phytoplankton bloom. *Journal of Marine Research*, *50*(2), 267–296. https://doi.org/10.1357/002224092784797692

Needoba, J. A., Sigman, D. M., & Harrison, P. J. (2004). The mechanism of isotope fractionation during algal nitrate assimilation as illuminated by the ^{15}N/^{14}N of intracellular nitrate. *Journal of Phycology*, *40*(3), 517–522. https://doi.org/10.1111/j.1529-8817.2004.03172.x

O'Leary, M. H. (1981). Carbon isotope fractionation in plants. *Phytochemistry*, *20*(4), 553–567. https://doi.org/10.1016/0031-9422(81)85134-5

Orsi, A. H., Whitworth, T., & Nowlin, W. D. (1995). On the meridional extent and fronts of the Antarctic Circumpolar Current. *Deep-Sea Research Part I*, *42*(5), 641–673. https://doi.org/10.1016/0967-0637(95)00021-W

Otero, X. L., De La Peña-Lastra, S., Pérez-Alberti, A., Ferreira, T. O., & Huerta-Diaz, M. A. (2018). Seabird colonies as important global drivers in the nitrogen and phosphorus cycles. *Nature Communications*, *9*(1), 246. https://doi.org/10.1038/s41467-017-02446-8

Paasche, E., Bryceson, I., & Tangen, K. (1984). Interspecific variation in dark nitrogen uptake by dinoflagellates 1. *Journal of Phycology*, *20*(3), 394–401. https://doi.org/10.1111/j.0022-3646.1984.00394.x

Pennock, J. R., Velinsky, D. J., Ludlam, J. M., Sharp, J. H., & Fogel, M. L. (1996). Isotopic fractionation of ammonium and nitrate during uptake by *Skeletonema costatum*: Implications for $\delta^{15}N$ dynamics under bloom conditions. *Limnology & Oceanography*, *41*(3), 451–459. https://doi.org/10.4319/lo.1996.41.3.0451

Planquette, H., Sanders, R. R., Statham, P. J., Morris, P. J., & Fones, G. R. (2011). Fluxes of particulate iron from the upper ocean around the Crozet Islands: A naturally iron-fertilized environment in the Southern Ocean. *Global Biogeochemical Cycles*, *25*(2). https://doi.org/10.1029/2010GB003789

Pollard, R. T., Salter, I., Sanders, R. J., Lucas, M. I., Moore, C. M., Mills, R. A., et al. (2009). Southern Ocean deep-water carbon export enhanced by natural iron fertilization. *Nature*, *457*(7229), 577–580. https://doi.org/10.1038/nature07716

Popp, B. N., Trull, T. W., Kenig, F., Wakeham, S. G., Rust, T. M., Tilbrook, B., et al. (1999). Controls on the carbon isotopic composition of southern ocean phytoplankton. *Global Biogeochemical Cycles*, *13*(4), 827–843. https://doi.org/10.1029/1999GB900041

Prakash, S., Ramesh, R., Sheshshayee, M. S., Mohan, R., & Sudhakar, M. (2015). Nitrogen uptake rates and f-ratios in the equatorial and southern Indian Ocean. *Current Science*, *108*(2), 239–245. https://doi.org/10.2307/24218163

Probyn, T. A. (1985). Nitrogen uptake by size-fractionated phytoplankton populations in the southern Benguela upwelling system. *Marine Ecology Progress Series. Oldendorf*, *22*(3), 249–258. https://doi.org/10.3354/meps022249

Rafter, P. A., Bagnell, A., DeVries, T., & Marconi, D. (2019). Dataset: Estimated nitrate $\delta^{15}N$ modeled using an ensemble of artificial neural networks (EANNs). https://doi.org/10.1575/1912/bco-dmo.768655.1

Rafter, P. A., DiFiore, P. J., & Sigman, D. M. (2013). Coupled nitrate nitrogen and oxygen isotopes and organic matter remineralization in the Southern and Pacific Oceans. *Journal of Geophysical Research: Oceans*, *118*(10), 4781–4794. https://doi.org/10.1002/jgrc.20316

Rau, G. H., Takahashi, T., Des Marais, D. J., Repeta, D. J., & Martin, J. H. (1992). The relationship between $\delta^{13}C$ of organic matter and $[CO_{2(aq)}]$ in ocean surface water: Data from a JGOFS site in the northeast Atlantic Ocean and a model. *Geochimica et Cosmochimica Acta*, *56*(3), 1413–1419. https://doi.org/10.1016/0016-7037(92)90073-R

Rau, G. H., Takahashi, T., Des Marais, D. J., & Sullivan, C. W. (1991). Particulate organic matter $\delta^{13}C$ variations across the Drake Passage. *Journal of Geophysical Research*, *96*(C8), 15131–15135. https://doi.org/10.1029/91JC01253

Rau, G. H., Takahashi, T., & Marais, D. J. D. (1989). Latitudinal variations in plankton $\delta^{13}C$: Implications for CO_2 and productivity in past oceans. *Nature*, *341*(6242), 516–518. https://doi.org/10.1038/341516a0

Raven, J. A., Cockell, C. S., & De La Rocha, C. L. (2008). The evolution of inorganic carbon concentrating mechanisms in photosynthesis. *Philosophical Transactions of the Royal Society B: Biological Sciences*, *363*(1504), 2641–2650. https://doi.org/10.1098/rstb.2008.0020

Raven, J. A., & Johnston, A. M. (1991). Mechanisms of inorganic-carbon acquisition in marine phytoplankton and their implications for the use of other resources. *Limnology & Oceanography*, *36*(8), 1701–1714. https://doi.org/10.4319/lo.1991.36.8.1701

R Core Team, Rf. (2018). *R: A language and environment for statistical computing*. R foundation for statistical computing Vienna.

Reynolds, C. S. (2006). *The ecology of phytoplankton*. Cambridge University Press.

Roeske, C. A., & O'Leary, M. H. (1984). Carbon isotope effects on enzyme-catalyzed carboxylation of ribulose bisphosphate. *Biochemistry*, *23*(25), 6275–6284. https://doi.org/10.1021/bi00320a058

Roukaerts, A., Cavagna, A., Fripiat, F., Lannuzel, D., Meiners, K. M., & Dehairs, F. (2016). Sea-ice algal primary production and nitrogen uptake rates off East Antarctica. *Deep Sea Research Part II: Topical Studies in Oceanography*, *131*, 140–149. https://doi.org/10.1016/j.dsr2.2015.08.007

Sambrotto, R. N., & Mace, B. J. (2000). Coupling of biological and physical regimes across the Antarctic Polar Front as reflected by nitrogen production and recycling. *Deep Sea Research Part II: Topical Studies in Oceanography*, *47*(15), 3339–3367. https://doi.org/10.1016/S0967-0645(00)00071-0

Schallenberg, C., Bestley, S., Klocker, A., Trull, T. W., Davies, D. M., Gault-Ringold, M., et al. (2018). Sustained upwelling of subsurface iron supplies seasonally persistent phytoplankton blooms around the southern Kerguelen plateau, Southern Ocean. *Journal of Geophysical Research: Oceans*, *123*(8), 5986–6003. https://doi.org/10.1029/2018JC013932

Schlitzer, R. (2002). Carbon export fluxes in the Southern Ocean: Results from inverse modeling and comparison with satellite-based estimates. *Deep Sea Research Part II: Topical Studies in Oceanography*, *49*(9), 1623–1644. https://doi.org/10.1016/S0967-0645(02)00004-8

Schlitzer, R. (2021). Ocean data view.

Shatova, O., Wing, S. R., Gault-Ringold, M., Wing, L., & Hoffmann, L. J. (2016). Seabird guano enhances phytoplankton production in the Southern Ocean. *Journal of Experimental Marine Biology and Ecology*, *483*, 74–87. https://doi.org/10.1016/j.jembe.2016.07.004

Sigman, D. M., Altabet, M. A., McCorkle, D. C., François, R., & Fischer, G. (1999). The $\delta^{15}N$ of nitrate in the southern ocean: Consumption of nitrate in surface waters. *Global Biogeochemical Cycles*, *13*(4), 1149–1166. https://doi.org/10.1029/1999GB900038

Sigman, D. M., Altabet, M. A., McCorkle, D. C., François, R., & Fischer, G. (2000). The $\delta^{15}N$ of nitrate in the Southern Ocean: Nitrogen cycling and circulation in the ocean interior. *Journal of Geophysical Research*, *105*(C8), 19599–19614. https://doi.org/10.1029/2000JC000265

Silfer, J. A., Engel, M. H., & Macko, S. A. (1992). Kinetic fractionation of stable carbon and nitrogen isotopes during peptide bond hydrolysis: Experimental evidence and geochemical implications. *Chemical Geology: Isotope Geoscience section*, *101*(3), 211–221. https://doi.org/10.1016/0009-2541(92)90003-N

Smart, S. M., Fawcett, S. E., Ren, H., Schiebel, R., Tompkins, E. M., Martínez-García, A., et al. (2020). The nitrogen isotopic composition of tissue and shell-bound organic matter of planktic Foraminifera in Southern Ocean surface waters. *Geochemistry, Geophysics, Geosystems*, *21*(2), e2019GC008440. https://doi.org/10.1029/2019GC008440

Smart, S. M., Fawcett, S. E., Thomalla, S. J., Weigand, M. A., Reason, C. J. C., & Sigman, D. M. (2015). Isotopic evidence for nitrification in the Antarctic winter mixed layer. *Global Biogeochemical Cycles*, *29*(4), 427–445. https://doi.org/10.1002/2014GB005013

Smith, S., Altieri, K., Mdutyana, M., Walker, D., Parrott, R., Gallie, S., et al. (2022). Biogeochemical controls on ammonium accumulation in the surface layer of the Southern Ocean. *Biogeosciences*, *19*(3), 715–741. https://doi.org/10.5194/bg-19-715-2022

Squire, V. A. (2022). Marginal ice zone dynamics. *Philosophical Transactions of the Royal Society A: Mathematical, Physical & Engineering Sciences*, *380*(2235), 20210266. https://doi.org/10.1098/rsta.2021.0266

Stirnimann, L., Bornman, T. G., Verheye, H. M., Bachèlery, M.-L., van der Poel, J., & Fawcett, S. E. (2021). Plankton community composition and productivity near the Subantarctic Prince Edward Islands archipelago in autumn. *Limnology & Oceanography*, *66*(12), 4140–4158. https://doi.org/10.1002/lno.11949

Stirnimann, L., & Fawcett, S. E. (2023). Isotope ratios, carbon and nitrogen concentrations, and phytoplankton composition data from the ACE expedition [Dataset]. Zenodo. https://doi.org/10.5281/zenodo.8422942.AGU: Global biogeochemical cycles

St John Glew, K., Espinasse, B., Hunt, B. P. V., Pakhomov, E. A., Bury, S. J., Pinkerton, M., et al. (2021). Isoscape models of the Southern Ocean: Predicting spatial and temporal variability in carbon and nitrogen isotope compositions of particulate organic matter. *Global Biogeochemical Cycles*, *35*(9), e2020GB006901. https://doi.org/10.1029/2020GB006901

Strickland, J. D. H., & Parsons, T. R. (1972). *A practical handbook of seawater analysis* (2nd ed., p. 167). Bulletin Fisheries Research Board of Canada. https://doi.org/10.25607/OBP-1791

Sunda, W. G., & Hardison, R. D. (2007). Ammonium uptake and growth limitation in marine phytoplankton. *Limnology & Oceanography*, *52*(6), 2496–2506. https://doi.org/10.4319/lo.2007.52.6.2496

Sunda, W. G., & Huntsman, S. A. (1997). Interrelated influence of iron, light and cell size on marine phytoplankton growth. *Nature*, *390*(6658), 389–392. https://doi.org/10.1038/37093

Swart, S., Thomalla, S.J., & Monteiro, P. M. S. (2015). The seasonal cycle of mixed layer dynamics and phytoplankton biomass in the sub-Antarctic Zone: A high-resolution glider experiment. *Journal of Marine Systems*, *147*, 103–115. https://doi.org/10.1016/j.jmarsys.2014.06.002

Tagliabue, A., & Arrigo, K. R. (2016). Decadal trends in air-sea CO_2 exchange in the Ross Sea (Antarctica). *Geophysical Research Letters*, *43*(10), 5271–5278. https://doi.org/10.1002/2016GL069071

Talley, L. D. (2011). *Descriptive physical oceanography: An introduction*. Academic press.

Tamelander, T., Kivimäe, C., Bellerby, R. G. J., Renaud, P. E., & Kristiansen, S. (2009). Base-line variations in stable isotope values in an Arctic marine ecosystem: Effects of carbon and nitrogen uptake by phytoplankton. *Hydrobiologia*, *630*(1), 63–73. https://doi.org/10.1007/s10750-009-9780-2

Timmermans, K. R., Stolte, W., & de Baar, H. J. W. (1994). Iron-mediated effects on nitrate reductase in marine phytoplankton. *Marine Biology*, *121*(2), 389–396. https://doi.org/10.1007/BF00346749

Timmermans, K. R., van der Wagt, B., & de Baar, H. J. W. (2004). Growth rates, half-saturation constants, and silicate, nitrate, and phosphate depletion in relation to iron availability of four large, open-ocean diatoms from the Southern Ocean. *Limnology & Oceanography*, *49*(6), 2141–2151. https://doi.org/10.4319/lo.2004.49.6.2141

Tortell, P. D., Long, M. C., Payne, C. D., Alderkamp, A.-C., Dutrieux, P., & Arrigo, K. R. (2012). Spatial distribution of pCO_2, ΔO_2/Ar and dimethylsulfide (DMS) in polynya waters and the sea ice zone of the Amundsen Sea, Antarctica. *Deep Sea Research Part II: Topical Studies in Oceanography*, *71–76*, 77–93. https://doi.org/10.1016/j.dsr2.2012.03.010

Tortell, P. D., Payne, C. D., Li, Y., Trimborn, S., Rost, B., Smith, W. O., et al. (2008). CO_2 sensitivity of Southern Ocean phytoplankton. *Geophysical Research Letters*, *35*(4). https://doi.org/10.1029/2007gl032583

Tortell, P. D., Reinfelder, J. R., & Morel, F. M. M. (1997). Active uptake of bicarbonate by diatoms. *Nature*, *390*(6657), 243–244. https://doi.org/10.1038/36765

Treibergs, L. A., Fawcett, S. E., Lomas, M. W., & Sigman, D. M. (2014). Nitrogen isotopic response of prokaryotic and eukaryotic phytoplankton to nitrate availability in Sargasso Sea surface waters. *Limnology & Oceanography*, *59*(3), 972–985. https://doi.org/10.4319/lo.2014.59.3.0972

Trull, T. W., & Armand, L. (2001). Insights into Southern Ocean carbon export from the $\delta^{13}C$ of particles and dissolved inorganic carbon during the SOIREE iron release experiment. *Deep Sea Research Part II: Topical Studies in Oceanography*, *48*(11), 2655–2680. https://doi.org/10.1016/S0967-0645(01)00013-3

Trull, T. W., Davies, D., & Casciotti, K. (2008). Insights into nutrient assimilation and export in naturally iron-fertilized waters of the Southern Ocean from nitrogen, carbon and oxygen isotopes. *Deep Sea Research Part II: Topical Studies in Oceanography*, *55*(5), 820–840. https://doi.org/10.1016/j.dsr2.2007.12.035

Tsuji, Y., Suzuki, I., & Shiraiwa, Y. (2009). Photosynthetic carbon assimilation in the coccolithophorid *Emiliania huxleyi* (Haptophyta): Evidence for the predominant operation of the C_3 cycle and the contribution of β-carboxylases to the active anaplerotic reaction. *Plant and Cell Physiology*, *50*(2), 318–329. https://doi.org/10.1093/pcp/pcn200

Tuerena, R. E., Ganeshram, R. S., Humphreys, M. P., Browning, T. J., Bouman, H., & Piotrowski, A. P. (2019). Isotopic fractionation of carbon during uptake by phytoplankton across the South Atlantic subtropical convergence. *Biogeosciences*, *16*(18), 3621–3635. https://doi.org/10.5194/bg-16-3621-2019

Uitz, J., Claustre, H., Morel, A., & Hooker, S. B. (2006). Vertical distribution of phytoplankton communities in open ocean: An assessment based on surface chlorophyll. *Journal of Geophysical Research*, *111*(C8). https://doi.org/10.1029/2005JC003207

UKMO. (2005). GHRSST level 4 OSTIA global foundation sea surface temperature analysis. *NASA Physical Oceanography DAAC*. https://doi.org/10.5067/GHOST-4FK01

van Leeuwe, M. A., Webb, A. L., Venables, H. J., Visser, R. J. W., Meredith, M. P., Elzenga, J. T. M., & Stefels, J. (2020). Annual patterns in phytoplankton phenology in Antarctic coastal waters explained by environmental drivers. *Limnology & Oceanography*, *65*(7), 1651–1668. https://doi.org/10.1002/lno.11477

Van Oostende, N., Fawcett, S. E., Marconi, D., Lueders-Dumont, J., Sabadel, A. J. M., Woodward, E. M. S., et al. (2017). Variation of summer phytoplankton community composition and its relationship to nitrate and regenerated nitrogen assimilation across the North Atlantic Ocean. *Deep Sea Research Part I: Oceanographic Research Papers*, *121*, 79–94. https://doi.org/10.1016/j.dsr.2016.12.012

van Rossum, G. (1995). *Python reference manual*. Department of Computer Science [CS]. (R 9525).

Verdy, A., & Mazloff, M. R. (2017). A data assimilating model for estimating Southern Ocean biogeochemistry. *Journal of Geophysical Research: Oceans*, *122*(9), 6968–6988. https://doi.org/10.1002/2016JC012650

Vidussi, F., Claustre, H., Manca, B. B., Luchetta, A., & Marty, J.-C. (2001). Phytoplankton pigment distribution in relation to upper thermocline circulation in the eastern Mediterranean Sea during winter. *Journal of Geophysical Research*, *106*(C9), 19939–19956. https://doi.org/10.1029/1999JC000308

Villinski, J. C., Hayes, J. M., Brassell, S. C., Riggert, V. L., & Dunbar, R. B. (2008). Sedimentary sterols as biogeochemical indicators in the Southern Ocean. *Organic Geochemistry*, *39*(5), 567–588. https://doi.org/10.1016/j.orggeochem.2008.01.009

Volk, T., & Hoffert, M. I. (1985). Ocean carbon pumps: Analysis of relative strengths and efficiencies in Ocean-driven atmospheric CO_2 changes. *The Carbon Cycle and Atmospheric CO_2: Natural Variations Archean to Present*, 99–110. https://doi.org/10.1029/GM032p0099

Wafar, M., L'Helguen, S., Raikar, V., Maguer, J.-F., & Corre, P. L. (2004). Nitrogen uptake by size-fractionated plankton in permanently well-mixed temperate coastal waters. *Journal of Plankton Research*, *26*(10), 1207–1218. https://doi.org/10.1093/plankt/fbh110

Wainright, S. C., Haney, J. C., Kerr, C., Golovkin, A. N., & Flint, M. V. (1998). Utilization of nitrogen derived from seabird guano by terrestrial and marine plants at St. Paul, Pribilof Islands, Bering Sea, Alaska. *Marine Biology*, *131*(1), 63–71. https://doi.org/10.1007/s002270050297

Walton, D. W. H., & Thomas, J. (2018). *Cruise report-Antarctic circumnavigation expedition (ACE) 20th December 2016-19th March 2017* (pp. 1–380). OpenAIRE.

West, J. B., Bowen, G. J., Dawson, T. E., & Tu, K. P. (2009). *Isoscapes: Understanding movement, pattern, and process on Earth through isotope mapping*. Springer.

Williams, T. J., Wagner, A. J., Sikes, E. L., & Martin, E. E. (2021). Evolution of the oceanic ^{13}C suess effect in the southeastern Indian Ocean between 1994 and 2018. *Geochemistry, Geophysics, Geosystems*, *22*(4), e2020GC009402. https://doi.org/10.1029/2020GC009402

Zhang, L., Altabet, M. A., Wu, T., & Hadas, O. (2007). Sensitive measurement of NH_4^+ $^{15}N/^{14}N$ ($\delta^{15}NH_4^+$) at natural abundance levels in fresh and saltwaters. *Analytical Chemistry*, *79*(14), 5297–5303. https://doi.org/10.1021/ac070106d

Zhang, R., Ma, Q., Chen, M., Zheng, M., Cao, J., & Qiu, Y. (2019). Nitrogen uptake regime regulated by ice melting during austral summer in the Prydz Bay, Antarctica. *Acta Oceanologica Sinica*, *38*(8), 1–7. https://doi.org/10.1007/s13131-019-1434-2